BIOPHYSICS

A mechanochemical model recapitulates distinct vertebrate gastrulation modes

Mattia Serra[1]*, Guillermo Serrano Nájera[2], Manli Chuai[2], Alex M. Plum[1], Sreejith Santhosh[1], Vamsi Spandan[3], Cornelis J. Weijer[2], L. Mahadevan[3,4]*

During vertebrate gastrulation, an embryo transforms from a layer of epithelial cells into a multilayered gastrula. This process requires the coordinated movements of hundreds to tens of thousands of cells, depending on the organism. In the chick embryo, patterns of actomyosin cables spanning several cells drive coordinated tissue flows. Here, we derive a minimal theoretical framework that couples actomyosin activity to global tissue flows. Our model predicts the onset and development of gastrulation flows in normal and experimentally perturbed chick embryos, mimicking different gastrulation modes as an active stress instability. Varying initial conditions and a parameter associated with active cell ingression, our model recapitulates distinct vertebrate gastrulation morphologies, consistent with recently published experiments in the chick embryo. Altogether, our results show how changes in the patterning of critical cell behaviors associated with different force-generating mechanisms contribute to distinct vertebrate gastrulation modes via a self-organizing mechanochemical process.

INTRODUCTION

Gastrulation is a highly conserved process in the development of all vertebrate embryos (*1*), with the chick being an extensively studied model because it is easily cultured and imaged. During gastrulation, the chick transforms from a layer of epithelial cells into a layered structure of three major embryonic tissues: the ectoderm, mesoderm, and endoderm. At the moment of egg-laying, the chick embryo contains around 30,000 cells organized in a circular epiblast that will give rise to the embryo proper (EP) surrounded by a ring of extraembryonic (EE) tissue. During the first few hours of development, signals from the EE tissues and the developing hypoblast induce cells to differentiate into mesendoderm precursors in a sickle-shaped domain at the posterior edge of the epiblast (Fig. 1A). These mesendoderm precursor cells undergo directed cell intercalations that result in a contraction of the mesendoderm tissue toward its central midline, followed by an extension in the anterior direction, forming the primitive streak (PS) (Fig. 1, A and B) (*2*–*6*). In the streak, mesendoderm precursor cells undergo an epithelial-to-mesenchymal transition (EMT), followed by their individual ingression and migration into the developing embryo to form various mesodermal and endodermal structures (*7*, *8*). These cell behaviors drive embryo-scale counter-rotating tissue flows that converge at the site of PS formation (Fig. 1B) (*9*, *10*).

Three cell-scale active force-generating processes drive tissue flows: (i) the outward migration of the cells attached to the vitelline membrane at the boundary of the embryo, (ii) the active intercalation of the mesendoderm precursors generating forces in the plane of the epiblast, and (iii) the ingression of mesendoderm cells in the streak, which attracts cells toward the streak and drives the out of plane motion. The variation in tissue flows and morphologies seen across vertebrate gastrulation, ranging from fish and amphibians via reptiles to amniotes such as chicks and humans, are due to differences in embryo geometry and the relative contributions of these three force-generating processes.

A major unresolved question is which mechanisms underlie the coordination of these large-scale reproducible tissue flows during gastrulation. The onset of directional intercalations in the chick embryo correlates with the appearance of oriented chains of aligned junctions containing high levels of active myosin II motor proteins, as detected through phosphorylated myosin light chain (pMLC) (Fig. 1, A, left, and C) (*2*, *3*). These supracellular chains of aligned cell junctions with high levels of active myosin are oriented in the direction of cell intercalation, indicating the appearance of a supracellular oriented organization (planar cell polarity) of intercalating cells (Fig. 1E at HH1 stage and fig. S9). As the PS extends, supracellular cables of highly active myosin reorient perpendicular to the midline (Fig. 1, A, right, D, and E at HH3). Figure 1E shows the orientation of actomyosin cables (bar orientation), the extent of alignment of multicellular cables (bar length) quantified by the pMLC anisotropy, and the active myosin strength quantified by pMLC intensity (bar color) on the whole embryo at EGK-XIV, HH1, and HH3. The pMLC anisotropy is quantified from the asymmetry of the Fourier power spectrum (*11*), calculated in a tiling pattern over the embryo, while myosin intensity is calculated as average intensity in the same tiles. For experimental details, see the recently published paper (*4*). The panels show a high increase of active myosin over time (see also fig. S10), and at HH3, the PS region has maximal pMLC intensity and maximal anisotropy perpendicular to the PS.

These actomyosin cables, first observed in the directional cell intercalation underlying germ-band extension in fruit fly embryogenesis (*12*, *13*), were thought to arise from signaling in the anterior-posterior patterning system (*14*, *15*). Recent work (*16*–*19*) suggests instead that actomyosin cables could self-organize in a tension-dependent manner, leading to spontaneous large-scale orientation during germ-band extension. Consistent with this, it is now well established that cytoskeletal actin dynamics, myosin activity, and

[1]Department of Physics, University of California San Diego, La Jolla, CA 92093, USA. [2]Division of Cell and Developmental Biology, College of Life Sciences, University of Dundee, Dundee DD1 5EH, UK. [3]School of Engineering and Applied Sciences, Harvard University, Cambridge, MA 02138, USA. [4]Departments of Physics, and Organismic and Evolutionary Biology, Harvard University, Cambridge, MA 02138, USA.
*Corresponding author. Email: mserra@ucsd.edu (M.S.); lmahadev@g.harvard.edu (L.M.)
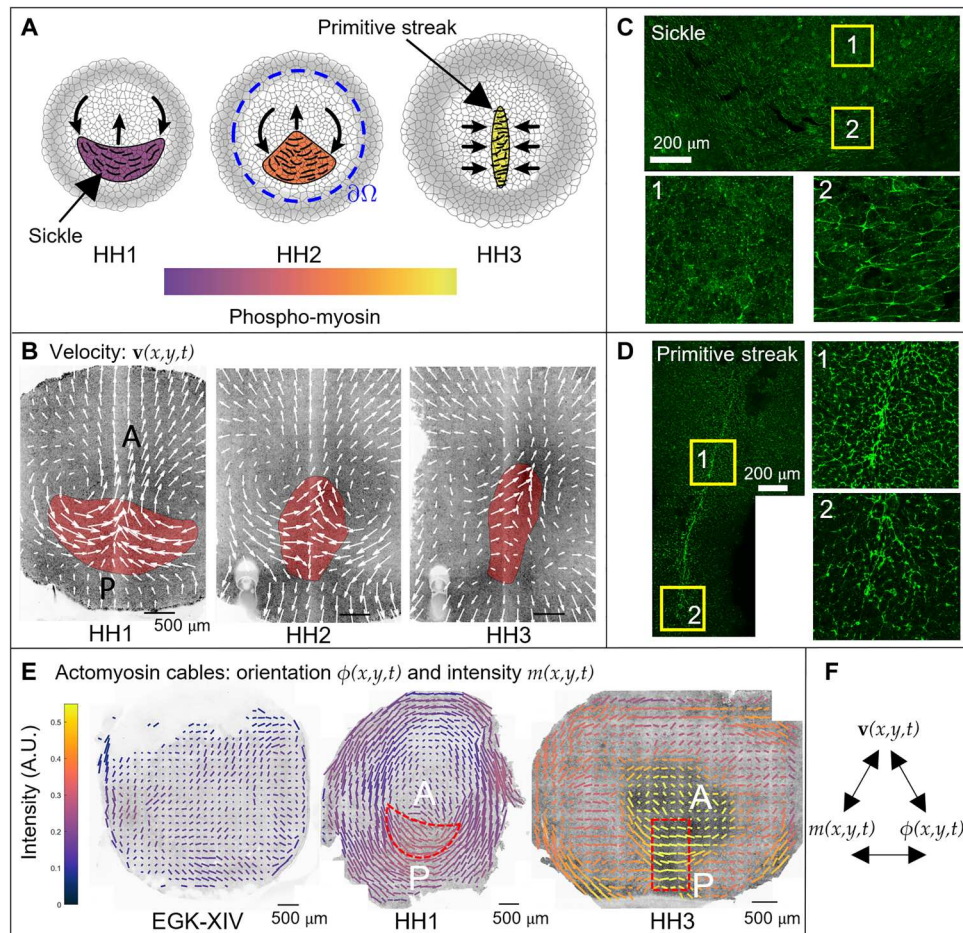
Fig. 1. Actomyosin cables drive the tissue flows in gastrulation. (**A**) PS formation diagram. (**B**) Velocity in the chick gastrula. The convergent extension of the mesendoderm (red) generates macroscopic tissue flows on the surface of the embryo. (**C**) At HH1, the mesendoderm sickle territory is characterized by supracellular cables with active myosin (phosphorylated myosin light chain; pMLC) perpendicular to the anterior-posterior (AP) direction (see fig. S9 for details). (**D**) At HH3—12 hours after HH1—the PS is characterized by supracellular cables with high active myosin (pMLC) perpendicular to the midline. (**E**) The pattern of actomyosin cables evolves from EGK-XIV to HH3. Bar lengths represent the pMLC anisotropy and bar colors represent the measured absolute concentration. The red dashed sickle and rectangle indicate the mesendoderm precursors region and a stripe of tissue containing the PS. At HH3, the PS region has maximal pMLC intensity and maximal anisotropy perpendicular to the PS, resulting in the highest active stress along cables perpendicular to the PS. Figure S10 shows the same measured pMLC signal intensity as a scalar field over the embryo, demonstrating an overall increase in myosin activity. For experimental details, see (*4*). (**F**) Here, we construct a theoretical framework coupling velocity, actomyosin orientation, and intensity that explains observed gastrulation flows in recent experiments.

adhesion are mechanosensitive (*20, 21*), e.g., contraction of a given junction will increase the tension of neighboring junctions, which in turn activates the myosin assembly and lowers the dissociation rate of active myosin in those junctions through a catch-bond mechanism (*22–24*). This positive feedback mechanism could then result in the formation of supracellular chains of myosin-enriched junctions at the cellular level that drive coordinated supracellular directional intercalations, organized tissue flows, and PS formation (*5*). In the chick, the early embryonic layer can be abstracted as a thin two-dimensional (2D) fluid in which myosin activity generates active stresses that induce multicellular flows. Interfering with myosin activity correlates with the failure of PS formation (*2, 4*). But what are the essential mechanisms sufficient to generate supracellular coordination?

To probe the conditions for the self-organization of actomyosin cables during development and correlate these with observed tissue flows, we need a quantitative predictive model. Theoretical approaches include statistical and continuum theories for active matter (*25*), vertex models (*26–28*), and constitutive laws for epithelia (*29*), with their relative strengths and weaknesses summarized in a recent review (*30*). Theoretical work has also started to elucidate the interplay of signaling, mechanics, and geometrical constraints (*31–40*) reviewed in (*41*). Here, we complement these studies and devise a continuum model that is specific enough to capture the essence of the distinct gastrulation modes we observed in wild-type and experimentally perturbed chick embryos while being general enough to apply to other morphogenetic processes.

Mathematical framework for gastrulation flows
Predictive model linking mechanochemical activity and tissue flows
Minimally, a planar mechanochemical predictive model of PS formation during gastrulation should couple three coarse-grained fields (Fig. 1F): the tissue velocity field $\mathbf{v}(x, y, t) = [u(x, y, t), v(x,$

$y, t)]^\top$, the active stress intensity $m(x, y, t)$ arising from myosin activity, and the average cable orientation $\phi(x, y, t)$. In the limit of slow, viscous flows associated with morphogenesis, we can neglect inertia so that the local force balance reads $\nabla \cdot \boldsymbol{\sigma}_T = \mathbf{0}$, where the total stress $\boldsymbol{\sigma}_T = \boldsymbol{\sigma}_V + \boldsymbol{\sigma}_A$ is the sum of the viscous and active stresses. The viscous stress is $\boldsymbol{\sigma}_V = -p\mathbf{I} + 2\mu\mathbf{S}_s$, where p is the pressure, $\mathbf{I}$ is the identity matrix, μ is shear viscosity, and $\mathbf{S}_s = (\nabla \mathbf{v} + \nabla \mathbf{v}^\top - (\nabla \cdot \mathbf{v})\mathbf{I})/2)$ is the deviatoric rate-of-strain tensor. The active stress associated with actomyosin cables is $\boldsymbol{\sigma}_A = m(\mathbf{B} - \mathbf{I}/2)$, with the components of $\mathbf{B}$ given by $B_{11} = \cos^2\phi$, $B_{12} = B_{21} = \sin 2\phi/2$, $B_{22} = \sin^2\phi$.

We model the sheet-like embryo as a two-dimensional compressible fluid to accommodate cell ingression into the third dimension. This necessitates a continuity law modeling the expectation that both the passive isotropic stress and isotropic effects of myosin activity contribute to a negative divergence (or convergence) of the local velocity field. We choose a simple linear model with $\nabla \cdot \mathbf{v} = c(-2p - p_0 m)$. Here, c^{-1} is the fluid bulk viscosity, $-2p$ is the isotropic viscous stress, and $p_0 m$ characterizes the effect of active cell ingression due to myosin-induced apical contraction (see sections S1.1 and S1.4.2 for a detailed description and the biophysical implications of p_0). This continuity law enables us to express the local pressure p as a function of $\nabla \cdot \mathbf{v}$ and m. Then, we may write the equations for local momentum balance for the planar velocity field $\mathbf{v}(x, y, t)$, along with the evolution equations for the orientation $\phi(x, y, t)$ and intensity $m(x, y, t)$ of active
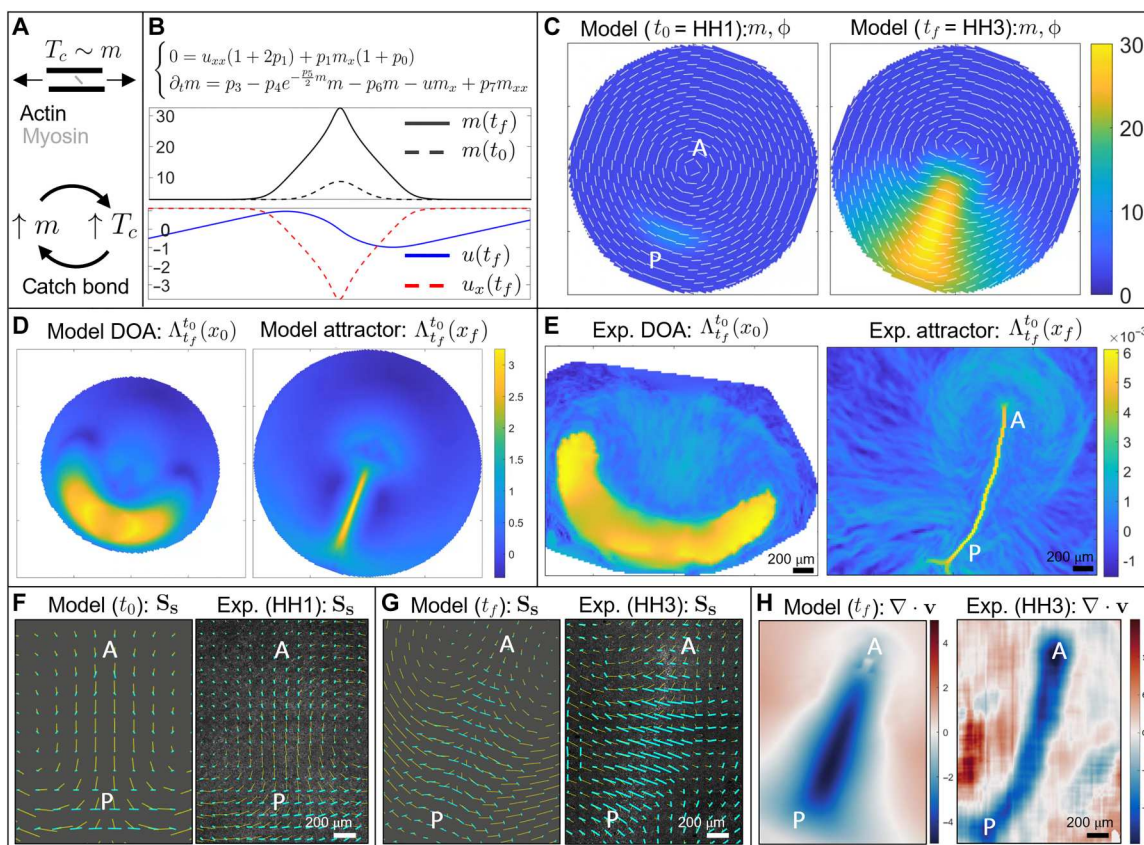

Fig. 2. Dynamics of wild-type gastrulation in the chick embryo. (**A**) In the gastrulation timescale, the tension in the actomyosin cables is maintained by their active stress intensity $T_c \approx \langle \mathbf{e}, \boldsymbol{\sigma}_A \mathbf{e} \rangle = m/2$ (section S1.3). High T_c induces a further increase of m via the catch-bond mechanism, which in turn increases T_c. This positive feedback process causes the instability of Eq. 1. (**B**) One-dimensional model recapitulates a focusing-type instability of active myosin, which induces a colocated velocity sink describing cell ingression at the PS. Movie S1 shows the time evolution of m, u, u_x. (**C**) Initial (t_0) and final (t_f) distributions of m, ϕ for the 2D model. The instability of m drives cable reorientation and active myosin evolution. These, in turn, drive the tissue flows underlying the extension of the streak from posterior (P) to anterior (A). (**D**) Model-based domain of attraction (DOA) at t_0 (HH1) and the attractor at t_f (HH3). Movie S2 shows the time evolution of the relevant model-based $\mathbf{v}$, m, ϕ, Lagrangian grid, repellers, DOAs, and attractors. (**E**) Same as (D) for the experimental velocity. Movie S3 shows the time evolution of the Lagrangian metrics for the experimental $\mathbf{v}$. Panel (E) adapted with permission from (44). (**F** and **G**) Line segments indicate the velocity (yellow) and contracting eigenvector of the deviatoric rate of strain tensor (cyan) with length proportional to the contraction strength. (F) Model-based and experimental velocity deviatoric rate of strain at HH1 (t_0). (G) Same as (F) at HH3 (t_f). The experimental panels' background consists of fluorescence images. (**H**) Model-based and experimental velocity divergence at HH3 (t_f). Color bars in (C), (D), and (H) (left) are in nondimensional units. Color bars in (E) and (H) (right) are in 1/minutes. See section S4.6 for parameters, boundaries, and initial conditions used in Eq. 1.

stress as

$$
\begin{cases}
\text{Force balance:} \\[2pt]
\overbrace{2p_1\Delta\mathbf{v}}^{\text{shear}} + \overbrace{\nabla[\nabla\cdot\mathbf{v}]}^{\text{dilatation}} + \overbrace{2p_1(\mathbf{B}\nabla m + m\nabla\cdot\mathbf{B}) + p_1(p_0-1)\nabla m}^{\text{active}} = 0 \quad (1a) \\[10pt]
\text{Dynamics of active stress orientation:} \\[2pt]
\phi_t = \overbrace{-(\mathbf{v}\cdot\nabla)\phi}^{\text{advection}} + \overbrace{\frac{\omega}{2}}^{\text{rigid rotation}} + \overbrace{p_2\left(\frac{u_y+v_x}{2}\cos2\phi + \frac{v_y-u_x}{2}\sin2\phi\right)}^{\text{shear}-\text{induced rotation}} \quad (1b) \\[10pt]
\text{Dynamics of active stress intensity:} \\[2pt]
m_t = \overbrace{-(\mathbf{v}\cdot\nabla)m}^{\text{advection}} + \overbrace{p_3}^{\text{recruitment}} \overbrace{-p_4 e^{-\frac{p_5}{2}m}m}^{\text{dissociation}} \overbrace{-p_6 m}^{\text{saturation}} + \overbrace{p_7\Delta_\phi m}^{\text{tension propagation}\rightarrow\text{induction of }m} \\[6pt]
\hspace{10cm} (1c)
\end{cases}
$$

Here, we have nondimensionalized our model using a characteristic length scale x_c, speed u_c, and viscous shear stress $\mu u_c/x_c$. Equation 1a denotes the balance of forces, wherein the first and second terms are the passive, viscous forces due to shear and dilatational deformations. The last three terms are a consequence of active forces induced by inhomogeneities in the active stress intensity generated by actomyosin cables, while $p_1 = \mu c$ is the ratio of the shear viscosity to the bulk viscosity (see section S1 for the derivation of these equations and fig. S11 for the effect of a higher ratio). Equation 1b describes the average orientational dynamics of active stress, dictated by the orientation of actomyosin cables which evolve like material fibers, advected by the flow, and rotated by vorticity ω and shear (42). Shear-induced rotation rates are modulated by the nondimensional parameter $p_2 \approx 1$ for elongated fibers.

Equation 1c describes the dynamics of active stress intensity. The first two terms account for cell motion (advection) and the recruitment of myosin from the cytoplasm, assumed to have a uniform constant concentration m_n, at scaled rate $p_3 = (t_p/t_r)(m_n x_c)/(\mu u_c)$. Here, t_r is the recruitment timescale and t_p is the timescale for converting active myosin into tissue-scale active stress. This complex process involves kinetic reactions, single cells, and multicellular mechanochemical operations (section S1.3). The third term models a tension (T_c)-dependent dissociation rate associated with catch-bond dynamics (Fig. 2A), which has an exponential form $p_4 e^{p_5 T_c}$ (23). Using a combination of experimental results, vertex models, and timescale arguments, in section S1.3, we show that at gastrulation (i.e., long) timescales, the tissue scale $T_c \approx m/2$. $p_4 = t_p/t_d$ is the ratio of t_p to the dissociation timescale, and $p_5 = (k_o\mu u_c)/x_c$ is the ratio of the characteristic shear stress of the system to the characteristic bonding stress k_o^{-1} between actin and myosin. The fourth term on the right side of the last equation ensures that active stress intensity does not accumulate without bounds. We add the simplest linear saturation term in $p_6 m$, where $p_6 = \chi t_p$ and we choose χ to set a saturation value $m_{\text{sat}} \approx p_3/p_6$. The precise mechanisms and functional form that control myosin saturation are beyond the scope of our model because we are interested in a finite-time developmental interval characterized by instability rather than an asymptotic equilibrium state. This is confirmed by the sensitivity analysis (section S4.3), showing that our results are robust to changes in p_6. Last, the viscoelastic behavior of the cables also results in the propagation of active stress intensity along the cable orientations, making the dynamics of active stress intensity non–cell autonomous (37). At the tissue scale, this results in directional diffusion of active stress intensity $\Delta_\phi m$ along the local cable orientation ϕ in Eq. 1c (see section S1.3 for derivation and section S3 for

visualization). $p_7 = \xi/(x_c u_c)$ is the ratio between the transport of active stress intensity via advection and induction of active stress intensity via cable tension propagation, where ξ captures the tissue-scale effect of tension propagation.

We note that the force balance (Eq. 1a) to determine $\mathbf{v}(x, y, t)$ is elliptic, i.e., $\mathbf{v}(x, y, t)$ at a particular location depends on $\mathbf{v}(x, y, t)$ throughout the embryo. Because $\mathbf{v}(x, y, t)$ affects $m(x, y, t)$, $\phi(x, y, t)$ (Eqs. 1b to 1c), the local active stress dynamics also depend on $\mathbf{v}$ in the whole embryo. In addition, the directional diffusion in the dynamics of the myosin field m makes the model non–cell autonomous even in Lagrangian coordinates, i.e., along cell trajectories. Since the chick embryo is roughly planar and circular, we solve Eq. 1 in polar coordinates by considering a circular spatial domain with boundary $\partial\Omega$ (Fig. 1A) that encloses the embryonic area and a small fraction of the EE region. This allows us to keep the size of the domain approximately fixed, as the embryonic area remains constant during gastrulation.

To complete the formulation of the problem, we need boundary and initial conditions. We impose a velocity normal to the boundary to represent epiboly and no flux for m, ϕ, as there is no experimental evidence of sources, sinks, or prescribed values of m, ϕ close to the EP-EE boundary. For details on model derivation, see sections S1.1 to S1.3. For nondimensionalization, see section S1.4. For the model in polar coordinates, see section S1.5. For the numerical scheme, see section S2. For parameter selection and sensitivity analysis, see section S4. The tension-dependent, non–cell-autonomous dynamics of actomyosin cables and the coupling of tissue compressibility to tissue stress and active myosin are two key aspects that our framework adds to the growing evidence accounting for feedback between mechanical and biochemical processes in development.

Quantification of spatiotemporal morphogenetic flows
To complement the theoretical model (Eq. 1) for the spatiotemporal patterning of actomyosin activity and flow, we also need a properly invariant approach to quantify the resulting 2D spatiotemporal flows and compare our model results with experiments. Any framework to analyze spatiotemporal trajectories in morphogenesis requires a self-consistent description of cell motion that is independent of the choice of reference frame. This frame-invariant property, called objectivity (43), is a fundamental requirement that ensures that the description of deforming biological tissue is independent of the coordinate frames we choose to describe its motion. Nonobjective metrics, such as cell velocities, will yield different (inconsistent) results if they are described from a frame moving with a drifting embryo or a fixed lab frame [see, e.g., figure 1 in (44)].

By contrast, Lagrangian coherent structures that lead to the notion of dynamic morphoskeletons (DMs) (44) are objective. The DM is based on a Lagrangian description (fig. S8A) of tissue deformation captured by finite-time Lyapunov exponents (FTLE), which combine local and global mechanisms along cell trajectories. The DM consists of attractors and repellers toward which cells converge or diverge over a specific time interval $T = t_f - t_0$. Repellers are marked by high values of the forward FTLE $\Lambda_{t_0}^{t_f}(\boldsymbol{x}_0)$; attractors are marked by high values of backward FTLE $\Lambda_{t_f}^{t_0}(\boldsymbol{x}_f)$ and their domain of attraction (DOA) by high values of the backward FTLE displayed on the initial cell positions $\Lambda_{t_f}^{t_0}(\boldsymbol{x}_0)$ (see section S6 for details and fig. S8B for an illustration). The DM reveals the organizers of

spatiotemporal trajectories and is robust to noise (*44*), hence it is ideal for quantifying morphogenesis and comparing models with experiments.

RESULTS

Insights from the 1D model

To gain intuition, we first analyze the 1D version of Eq. 1 modeling the dynamics perpendicular to AP, as summarized in Fig. 2B (section S1.4.3). Linear stability analysis of uniform equilibria of m reveals that the lower equilibrium is linearly stable, the intermediate equilibrium is linearly unstable, and the higher equilibrium—set by the linear saturation term—is linearly stable (fig. S3). Initializing the nonlinear system with a Gaussian perturbation $m(\mathbf{x}, t_0)$ near the unstable equilibrium (mimicking the onset of actomyosin cables in the sickle as in Fig. 1, A, C, and E), we see that our model develops a focusing-type instability which increases $m(\mathbf{x}, t_f)$ while generating a highly compressive region $u_x(t_f) \ll 0$, representing cell ingression at the streak. This process shows that a region with higher initial active stress intensity provided by higher myosin induces more tension along actomyosin cables (Fig. 2A), which results in the recruitment of more active myosin, thus increasing the active stress intensity via the positive feedback mechanism embodied in Eq. 1c. Movie S1 shows the time evolution of the relevant fields. While this simplified 1D model neglects cable orientations, it accounts for the important roles of both the catch-bond dynamics coupled with the flow field, and our effective constitutive law, both of which carry over to the 2D model. However, without accounting for the dynamics of actomyosin cable reorientation, this simple 1D model cannot reproduce the 2D patterns of convergent extension and vortical flows observed in experiments.

The 2D model predicts epiblast tissue flows during chick gastrulation

We initialize the 2D model with $m(\mathbf{x}, t_0)$ consisting of a curved Gaussian perturbation to the unstable equilibrium of m, mimicking the sickle-shaped region of mesendoderm precursors, and $\phi(\mathbf{x}, t_0)$ in the azimuthal direction (Fig. 2C), consistent with experiments (Fig. 1E at HH1) (*4*). See fig. S12 for the effects of varying the initial extent of this region. We note that understanding what sets these initial conditions is beyond the scope of this work. The instability of m drives both the flow velocity and cable orientations shown in Fig. 2C and movie S2, reproducing the typical flow patterns observed in wild-type experiments. This instability mechanism is consistent with experimental observations of increasing pMLC between HH1 and HH3 (Fig. 1E and fig. S10) (*4*). A closer look at m, ϕ shows that while at t_0 the active stress creates convergence perpendicular to the PS in the posterior, at later times, the active stress is dominant close to the PS (Fig. 2C), consistent with experiments. Figure 1E at HH3 quantitatively shows that pMLC has the highest intensity and pMLC anisotropy perpendicular to the PS, resulting in the highest active stress in the PS region, as predicted by Fig. 2C.

We now deploy the DM to quantify whether the Eulerian fields predicted by Eq. 1 at different times will properly integrate along cell paths, reproducing the observed morphogenetic features. In Fig. 2 (D and E), we show the DOA (left) and the attractor (right), corresponding to the largest time T in both the model and the experimental $\mathbf{v}$. The attractor marks the formed PS at HH3, while the

DOA marks the initial (HH1) position of cells that will end up in the PS. Movie S2 shows the time evolution of the model-based $\mathbf{v}$, m, ϕ, Lagrangian grid, repellers, DOAs, and attractors as T increases, while movie S3 shows the same Lagrangian quantities obtained from the experimental velocity field. Consistent with our model, figure 1 (A to G) and movie S2 of (*4*) show bright-field images and gene expression patterns that indicate the mesendoderm territory.

As an additional model-experiment comparison, we consider the objective Eulerian quantities $\mathbf{S}_s$ and $\nabla \cdot \mathbf{v}$. The cyan direction field in Fig. 2 (F and G) shows the contracting eigenvector field with the bar length proportional to the contraction strength (i.e., the corresponding eigenvalue) of the deviatoric rate of strain tensor $\mathbf{S}_s$ at HH1 and HH3. The contracting direction of $\mathbf{S}_s$ and its strength are a proxy of cell intercalation, consistent with dedicated intercalation analysis in figure 4 of (*4*). These results show that at HH1 (Fig. 2F), intercalation is perpendicular to the AP direction and dominant in the sickle-shaped domain at the posterior edge of the epiblast, while at HH3 (Fig. 2G) it is perpendicular to the entire PS. At HH3, the PS region is characterized by high cell ingression, resulting in highly negative planar divergence $\nabla \cdot \mathbf{v}$, while the rest of the embryo has positive divergence to ensure embryonic area homeostasis. Our model predicts these results in Fig. 2H (left), consistent with experiments in Fig. 2H (right). This match of the model and experiment at the final time (HH3) supports further our simple continuity law $\nabla \cdot \mathbf{v} = c(-2p - p_0 m)$.

However, we emphasize that matching Eulerian snapshots of $\mathbf{S}_s$ and $\nabla \cdot \mathbf{v}$ between the model and experiments is not sufficient, as it is their cumulative effect along cell trajectories that quantifies morphogenesis (*44*). This Lagrangian sum differs from a sum at a fixed Eulerian location [as explained in detail, e.g., in section S2C of (*44*)]. For example, the DOA in Fig. 2 (D and E) marks the initial (HH1) position of cells that will eventually ingress in the PS by HH3, which results from the Lagrangian sum of $\nabla \cdot \mathbf{v}$ along cell trajectories. In section S4, we discuss the selection of parameters, boundaries, and initial conditions using experiments and numerical simulations and show with an extensive sensitivity analysis (movies S14 to S27) that our results are robust to parameter variations.

Model-experiment comparison of active forces

Figure 1E shows that active stress is dominant in the posterior sickle-shaped domain at HH1, while at HH3, it is dominant in the PS region, consistent with our model predictions in Fig. 2C. To support this finding further, Fig. 3 compares the active forces $\mathbf{F}_A$ inferred indirectly from the Particle Image Velocimetry (PIV) velocities with those generated by Eq. 1. To infer the experimental $\mathbf{F}_A$, we use the general force balance for highly viscous active flows (as in Eq. 1a) $\mathbf{F}_A + \mathbf{F}_V = 0$, where $\mathbf{F}_V$ denotes the viscous, passive force. This implies that $\mathbf{F}_A = -\mathbf{F}_V = -(\nabla[\nabla \cdot \mathbf{v}] + 2p_1\Delta\mathbf{v})$, where the right-hand side can be evaluated from experimental velocities. Figure 3A outlines the experimental distribution of active force $\mathbf{F}_A$ from Fig. 3B over the corresponding fluorescence images.

At HH1, PIV-inferred active forces (Fig. 3B, top) are higher in the posterior sickle-shaped domain and point toward the AP axis, as predicted by our model (Fig. 3C, top). The model-based force is symmetric with respect to the AP direction. The asymmetry of the experimentally inferred active force has no effect on gastrulation except for slightly bending the PS to the left (Fig. 2E). At HH3, PIV-inferred active forces are dominant and perpendicular to the
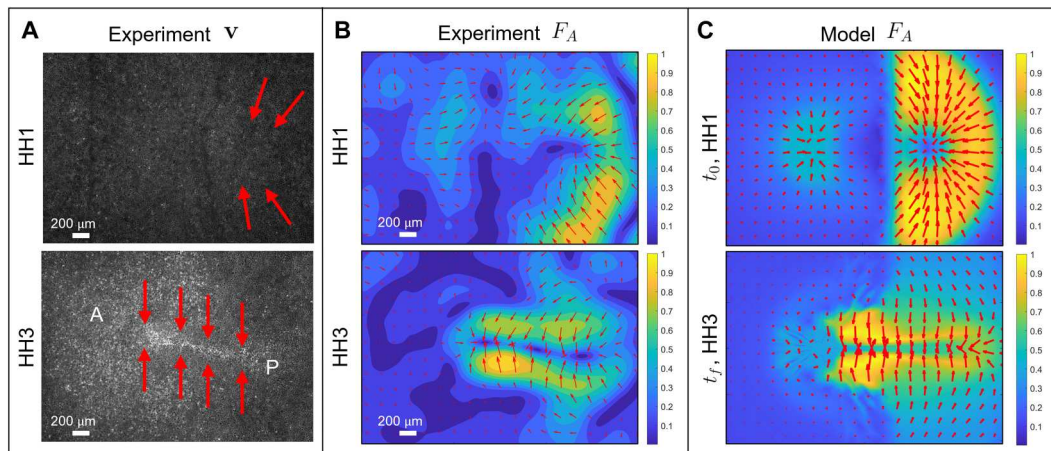
Fig. 3. Active forces in the chick embryo. (**A**) Experimental fluorescence images at HH1 and HH3. A and P mark the anterior-posterior direction, and red arrows illustrate the dominant active force $\mathbf{F_A}$ distribution from (**B**). At HH1, $\mathbf{F_A}$ is dominant in the posterior embryonic region perpendicular to the AP axis. At HH3, $\mathbf{F_A}$ is perpendicular to the PS throughout the AP axis. These $\mathbf{F_A}$ configurations are consistent with the corresponding distribution of supracellular actomyosin cables in Fig. 1E. Dimensions are 1300 μm × 1900 μm. (B) and (**C**) Magnitude and direction of forces at HH1 (top) and HH3 (bottom). Magnitudes are normalized by the maximal spatial force. (B) We compute $\mathbf{F_A}$ from the general force balance for highly viscous active flows $\mathbf{F_A} + \mathbf{F_V} = 0$ (cf. Eq. 1a), which gives $\mathbf{F_A} = -(\nabla[\nabla \cdot \boldsymbol{v}] + 2p_1\Delta\boldsymbol{v})$, where the right-hand side can be computed using experimental velocities. We use an averaging filter in space (window size ≈25 μm) and time (window size ≈15 min) on the PIV velocities and compute velocity derivatives using finite differencing. (C) $\mathbf{F_A}$ is from Eq. 1a. We note that the model $\mathbf{F_A}$ at HH3 arises from the dynamical variables evolved by Eq. 1 over the entire gastrulation period. They closely predict the corresponding inferred experimental forces [(B) bottom], further validating our model.

elongated PS region (Fig. 3B, bottom), as predicted by our model (Fig. 3C, bottom). This experimental evidence, consistent with the distribution pMLC in Fig. 1E and the corresponding model predictions (Figs. 2C and 3C), demonstrates that at least in the chick, active forces are not restricted to a ring-shaped structure at the EP-EE boundary, as suggested to be the case in the quail (3).

The model predicts perturbations
To further test our model predictions, we move beyond gastrulation in wild-type avian embryos and introduce four different perturbations that modify either the initial state of the embryonic pattern (i.e., region of mesendoderm precursors) characterized by high phosphorylated myosin and hence active stress intensity $m(\mathbf{x}, t_0)$, or the propensity for active cell ingression encoded in p_0. In section S4.6, we summarize the values of $m(\mathbf{x}, t_0)$ and p_0 used to reproduce different gastrulation modes. The rest of the parameters are the same for all simulations in the paper (section S4.6 and table S2).

Twin perturbation
Occasionally, a natural event corresponding to the spontaneous formation of twins arises when the mesendoderm precursor area is split into two regions, from which two streaks emerge. These streaks interact through their tissue flows and form complete or partially twined embryos (Fig. 4, A and B). We initialize our model as in the wild type (Fig. 2C) but add two distant Gaussians to the uniform unstable equilibrium of m. Movie S4 shows the model-based Eulerian fields and the induced Lagrangian metrics for increasing T. Figure 4A shows the model-based repeller and the attractor for the largest T. The circular repeller separates the EP from the EE region as well as the A-P regions of the PS, while the attractor marks the merging PSs. Figure 4B and movie S5 show the same as Fig. 4A and movie S4 for the experimental $\mathbf{v}$. A comparison of movies S4 and S5 highlights how our model recapitulates the full

morphogenetic process quantified by the DM. See fig. S13 for model predictions when PSs form opposite one another and for when one Gaussian has a greater amplitude than the other.

Reptilian-like mode
In the second perturbation, described in detail in the recently published paper (4), we interfered with a signaling pathway, which resulted in a strong inhibition of cell ingression in the streak, via the application of the VEGF receptor (vascular epithelial growth factor) inhibitor axitinib (100 nM). We initialize our model as in the wild type (Fig. 2C) but set $p_0 = 0$ as Axitinib prevents active cell ingression. Figure 4 (C and D) shows the DOA and attractor for both the model and experimental $\mathbf{v}$, highlighting how this perturbation results in a shorter and thicker PS as well as a reduced amount of ingressed cells, consistent with the bright-field images and gene expression patterns in figure 2 (H to N) of (4). Movies S6 and S7 show the time evolution of the model- and experiment-based fields confirming similar DM again.

Teleost-like mode
The third perturbation consists of experiments where FGF2 (fibroblast growth factor 2) addition to early-stage chick embryos provoked the generation of a mesoderm ring along the marginal zone (4). To model this case, we use the same conditions as the wild type but set $m(\mathbf{x}, t_0)$ as a Gaussian around a fixed radius added to the unstable equilibrium [see $m(\mathbf{x}, t_0)$ in movie S8]. Figure 4 (E and F) shows the DOA and attractor corresponding to the largest T from the model and experimental $\mathbf{v}$, highlighting a sharp circular PS. Movies S8 and S9 show the Eulerian fields and the Lagrangian metrics from the model and experimental $\mathbf{v}$ for increasing T. In addition, Movie S10 shows a deforming Lagrangian grid overlaid on the light-sheet microscope images. These results complement those in figure 1 (H to N) of (4) and confirm again the predictive power of our model.
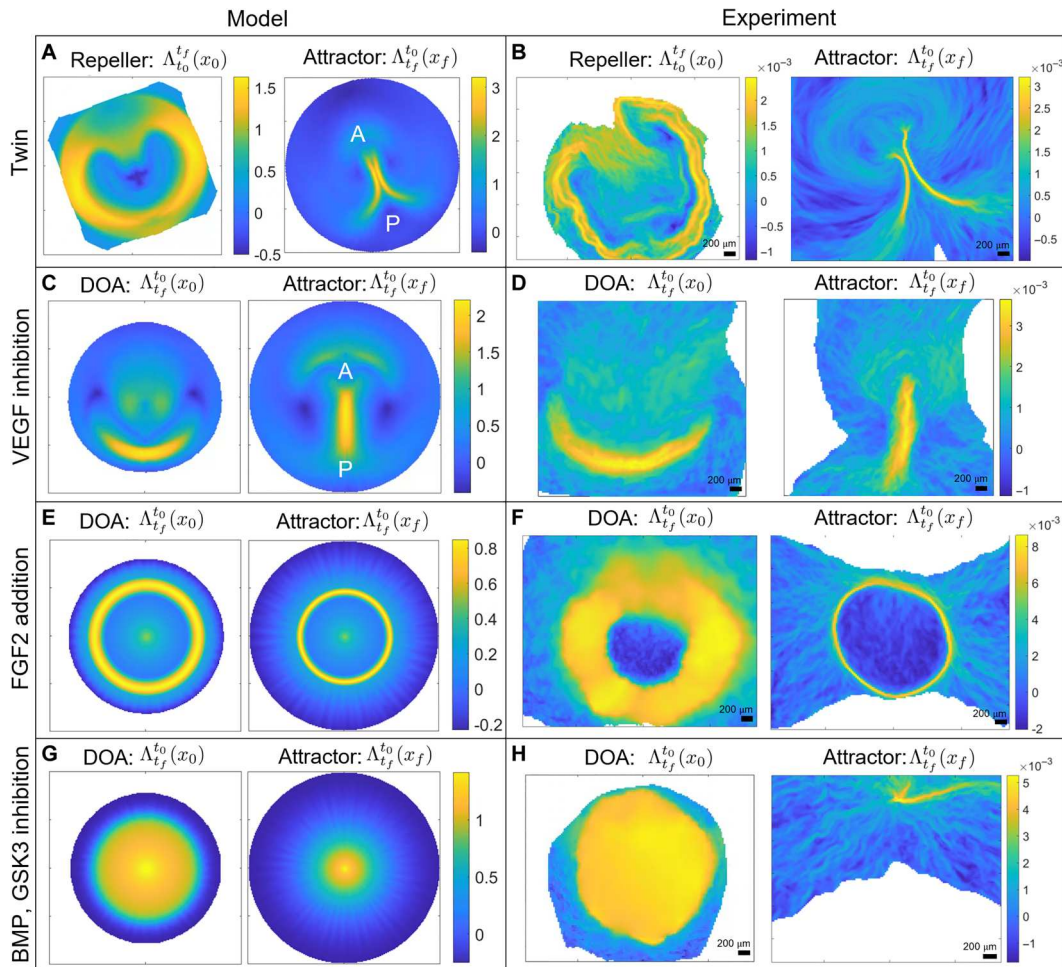
Fig. 4. Developmental perturbations of gastrulation. Movies show the time evolution of the relevant Eulerian and Lagrangian metrics. (**A** and **B**) Spontaneous twin perturbation. Repeller and attractor for model velocities [(A), movie S4] and experimental velocities [(B), movie S5]. (**C** and **D**) VEGF (vascular epithelial growth factor) inhibition prevents cell ingression at the PS. DOA and attractor for model velocities [(C), movie S6] and experimental velocities [(D), movie S7]. (**E** and **F**) FGF2 (fibroblast growth factor 2) addition provokes a circular PS. DOA and attractor for model velocities [(E), movie S8] and experimental velocities [(F), movie S9]. (**G** and **H**) BMP (bone morphogenetic protein) and GSK3 (glycogen synthase kinase 3) inhibition induce a ring-shaped mesoderm territory at the EE-EP interface while blocking apical contraction and cell ingression. DOA and attractor for model velocities [(G), movie S11) and experimental velocities [(H), movie S12]. Color bars in experimental panels show attraction rates in 1/minutes. See section S4.6 for parameters values, boundaries, and initial conditions used in simulating Eq. 1.

Amphibian-like mode

In our last perturbation, we induced the formation of a ring-shaped mesoderm region at the EE-EP interface with a combination of the BMP (bone morphogenetic protein) receptor inhibitor LDN-193189 (100 nM) and the GSK3 (glycogen synthase kinase 3) inhibitor CHIR-99021 (3 μM) (*4*). This treatment also blocks apical contraction and cell ingression but has little effect on cell intercalations, resulting in the buckling of the tissue [figure 2 (A to G) and movie S8 of (*4*)]. In our model, we use the initial condition of perturbation 3 but set $p_0 = 0$, following the same reasoning of perturbation 2. Figure 4 (G and H) shows the DOA and the attractor for the largest T from the model and the experimental **v**, while movies S11 and S12 display the corresponding time evolution of the Eulerian fields and Lagrangian metrics. While tissue buckling is intrinsically 3D, our model is sufficient to predict an overall planar compressive stress that causes the tissue to converge in the center.

This prediction matches precisely the experimental 2D dynamics inferred by PIV velocities.

Toward a phase space of gastrulation flow patterns

To go beyond studying the gastrulation modes in wild-type avian embryos exemplified by the chick, we used chemical inhibitors to uncouple cell intercalation and ingression and perturb the initial patterning and function of the prospective mesendoderm, as described in our recently published experimental paper (*4*). The current paper shows that we can recapitulate these phylogenetic variations in the morphodynamics of vertebrate gastrulation using a mechanochemical model that couples the dynamics of actomyosin cables to large-scale tissue flow patterns. By changing the cell's propensity to undergo active ingression from apical isotropic myosin contraction, characterized by the parameter p_0, together with the initial prospective mesendoderm, described by $m(\mathbf{x}, t_0)$ (Fig. 5, left), we can predict distinct gastrulation flows that resemble those

naturally observed in other vertebrates, consistent with in vivo experiments in the chick embryo (Fig. 5, center right). Specifically, the PS structures in Fig. 4 (C and D) resemble the blastoporal canal observed in reptilian gastrulation (Fig. 5, second row), the circular streak structure (Fig. 4, E and F) resembles the germ ring of teleost fish gastrulation (Fig. 5, last row), while the buckling tissue in Fig. 4 (G and H) mimics the tissue organization and flow during the closing blastopore in amphibians (Fig. 5, third row). We highlight that our biophysical model is sufficient to explain both the wild-type and manipulated gastrulation flows in the chick embryo, which show remarkable similarities to the gastrulation patterns naturally observed in other species. Whether our framework can explain (at least partially) the gastrulation flows in different vertebrates is a separate biological question that requires additional work (45).

DISCUSSION

In this study, we have investigated the self-organizing principles of gastrulation flows in wild-type and experimentally perturbed chick embryos. Using in vivo experiments and biophysical modeling, we have provided evidence that gastrulation movements arise from the coupled dynamics of tissue flows and mechanosensitive actomyosin activity (Eq. 1). Actomyosin activity generates active stresses, which drive tissue flows and tension. Tissue flows and tension, in turn, modulate actomyosin (or active stress) dynamics with mechanochemical feedback. Specifically, the actomyosin dissociation rate depends on the tissue-scale tension via a catch-bond mechanism, while tissue flows modulate actomyosin cable orientation. Because of the induction of active stress intensity via tension propagation, our model is non–cell-autonomous even in Lagrangian coordinates that follow cell trajectories. Our framework shows that gastrulation flows follow from an active stress instability (Fig. 2), consistent with experiments (Fig. 1 and fig. S10).
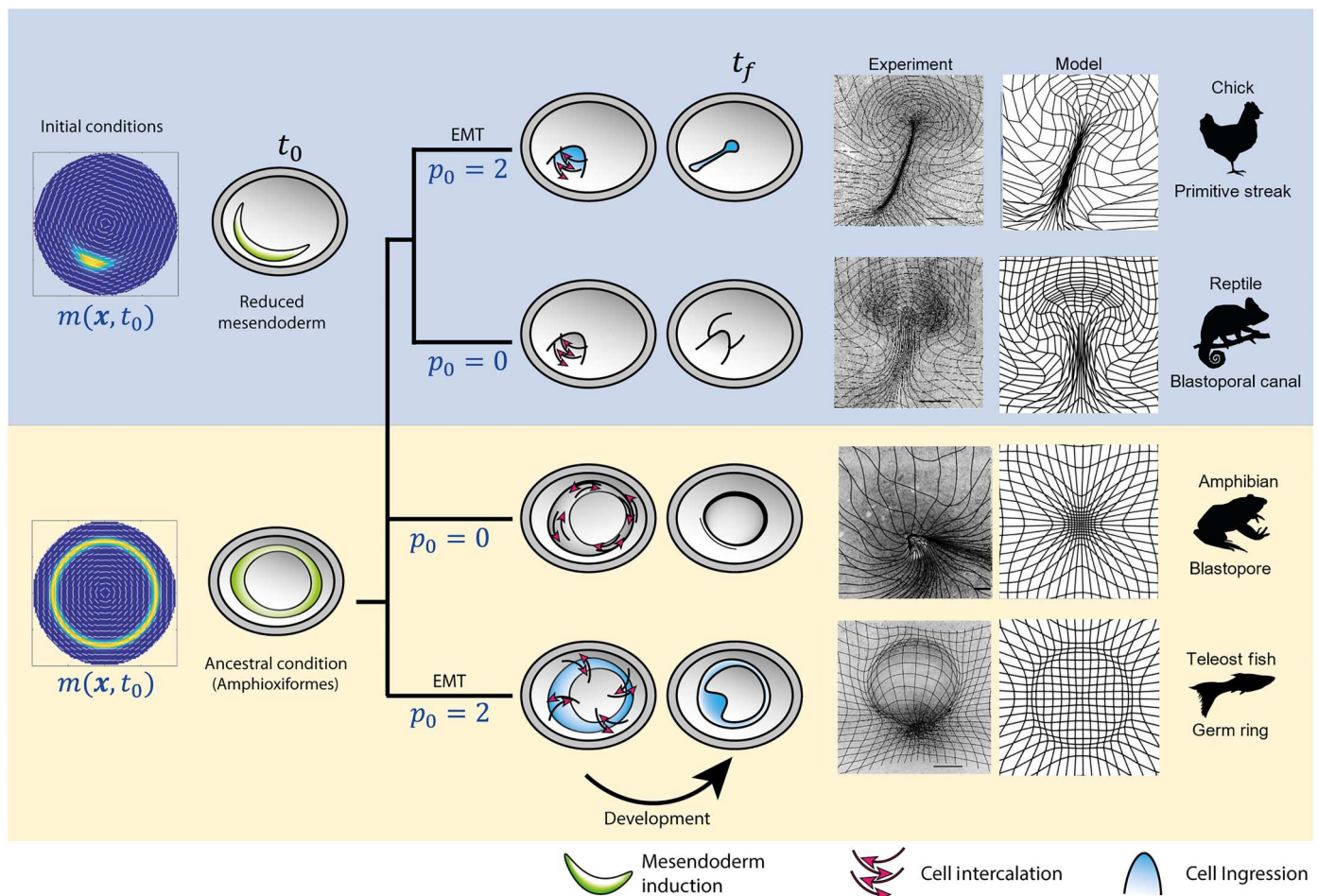
Fig. 5. Evolutionary transitions in gastrulation patterns. A critical morphogenetic parameter p_0 models the amount of EMT or active cell ingression caused by the cell's propensity to ingress given apical myosin-induced isotropic contraction. The initial condition $m(\mathbf{x}, t_0)$ models the extent of the mesendoderm precursor territory. Changing cell behaviors p_0 and initial cell types $m(\mathbf{x}, t_0)$ (left column), our model recapitulates the flow patterns in the phylogeny of vertebrate gastrulation from a self-organizing dynamical structure. Our model-based predicted flow patterns mimic those naturally observed in reptiles, amphibians, and fish, and are reproduced experimentally, in vivo, in the chick embryo [see also the recently published paper (4) for details on the experiments]. The right columns show deformed Lagrangian grids overlaying the light-sheet microscope images from perturbed chick-experiment velocities (4) and deformed Lagrangian grids from the predicted model velocity for each gastrulation mode. Scale bars, 500 μm.

In particular, providing only the initial conditions for the acto-myosin cables at the onset of chick gastrulation and the boundary conditions modeling the epiboly motion of EE cells, our model predicts subsequent gastrulation stages over 12 hours (Figs. 2 and 4 and movies S2 to S12). This allows us to recapitulate the observed dynamics of actomyosin cable reorientation, as well as the redistribution of actomyosin levels (Fig. 1E and fig. S10), the observed active forces, and the large-scale tissue motion. The experimental distribution of actomyosin cables (Fig. 1E) and the active forces inferred from PIV velocities (Fig. 3) show that in chick, active forces are not organized in a ring-shaped structure at the boundary between embryonic and EE regions, as suggested to be the case in the quail (3). In fact, at late gastrulation stages, active forces dominate in the PS region at the embryo's midline (Fig. 3). While Saadaoui et al. (3) and Caldarelli et al. (46) directly prescribe active forces on a tensile ring located at the boundary between the EP and EE area, our active force distribution evolves spontaneously in space and time through Eq. 1, leading to a self-organized pattern consistent with experiments (Figs. 1E and 3B). Furthermore, our framework predicts the velocity divergence and other dynamical fields (Fig. 2 and movies S2 to S12) from the underlying self-organizing dynamics in contrast to (3, 46) that fits spatiotemporal experimental velocity divergence fields into the model. A detailed comparison with the tensile-ring model is given in section S5.

By changing a nondimensional parameter modeling active cell ingression (cell behavior)—i.e., the cell's propensity to ingress due to high myosin-induced apical contraction—together with the initial distribution of active myosin as a proxy of prospective mesendoderm tissue (cell type), our model recapitulates distinct gastrulation flows that mimic those observed in fish, amphibians, and reptiles, consistent with experiment in vivo in the chick embryo (Fig. 5). In the recently published paper (4), we used drugs to modulate the ability for active cell ingression and the initial extent of the prospective mesendoderm and showed that the resulting gastrulation flows mirror those naturally observed in reptiles, amphibians, and fish in a single organism, the chick embryo, consistent with our model predictions. Additional or alternative driving forces may be at play in these other species (45). For example, studies of amphibian gastrulation in Xenopus have suggested that convergent thickening serves as an additional driving force during blastopore closure (47–49). Studies of teleost fish gastrulation in zebrafish have suggested that active directed cell migration of mesendoderm precursors plays an important role in their internalization (50, 51). Therefore, while the driving forces we have modeled are sufficient to generate flows in chick that mirror gastrulation in these other species, the exact gastrulation mechanisms in other vertebrates likely involve additional forces, not yet directly captured in our model.

To estimate the scalar, time-independent nondimensional parameters in our model, we use a combination of mechanistic arguments, experiments, and numerical simulations. We also perform an extensive sensitivity analysis showing the robustness of our results to parameter variations (section S4 and movies S14 to S27). Although our model does not account for 3D effects, the multilayered structure of EE tissue, different cell types, and the overall size and shape of embryos, we capture the essential differences in the modes of tissue flow in a range of vertebrate gastrulation. The consistency of our predictions with in vivo experiments in the chick embryo shows that a relatively small number of changes in critical cell behaviors associated with different force-generating processes contribute to the outcome of distinct vertebrate gastrulation modes via a self-organizing mechanism. The simplicity of the perturbations suggests that these divergent gastrulation morphologies might be relatively easily evolvable. A natural next step is to account for the above limitations, starting from different embryo sizes and geometries, modeling 3D effects, and explicitly accounting for distinct cell types to link tissue flows and morphogenesis with cell differentiation.

Linking the gene expression patterns to the myosin patterns and cell flows is an important step to fully understand the early stages of development. In principle, we already have the tools to map gene expression patterns on the cell flows using the Lagrangian DM framework (44). This mapping will allow us to couple the deformation of the gene expression domains responsible for mesendoderm induction and maintenance while ensuring further mesoderm and endoderm specification and spatial organization. These processes likely result in further changes in stress generation and mechanical feedback, completing the current theoretical framework of early chick development.

MATERIALS AND METHODS
For details on the acquisition and processing of the experimental data used in this work, please see the material and methods section of our accompanying paper (4). A detailed description of the numerical schemes used to solve our model (Eq. 1) is in section S2. The numerical scheme to compute the DMs from experimental and modeled velocity fields is in section S6.

Supplementary Materials
This PDF file includes:
Supplementary Text
Figs. S1 to S13
Tables S1 to S3
Legends for movies S1 to S27
References

Other Supplementary Material for this manuscript includes the following:
Movies S1 to S27

REFERENCES AND NOTES
1. C. D. Stern, *Gastrulation: From Cells to Embryo* (CSHL Press, 2004).
2. E. Rozbicki, M. Chuai, A. I. Karjalainen, F. Song, H. M. Sang, R. Martin, H. J. Knölker, M. P. MacDonald, C. J. Weijer, Myosin-II-mediated cell shape changes and cell intercalation contribute to primitive streak formation. *Nat. Cell Biol.* **17**, 397–408 (2015).
3. M. Saadaoui, D. Rocancourt, J. Roussel, F. Corson, J. Gros, A tensile ring drives tissue flows to shape the gastrulating amniote embryo. *Science* **367**, 453–458 (2020).
4. M. Chuai, G. S. Nájera, M. Serra, L. Mahadevan, C. J. Weijer, Reconstruction of distinct vertebrate gastrulation modes via modulation of key cell behaviors in the chick embryo. *Sci. Adv.* **9**, eabn5429 (2023).
5. G. Serrano Nájera, C. J. Weijer, Cellular processes driving gastrulation in the avian embryo. *Mech. Dev.* **163**, 103624 (2020).
6. O. Voiculescu, F. Bertocchini, L. Wolpert, R. E. Keller, C. D. Stern, The amniote primitive streak is defined by epithelial cell intercalation before gastrulation. *Nature* **449**, 1049–1052 (2007).
7. Y. Nakaya, E. W. Sukowati, Y. Wu, G. Sheng, RhoA and microtubule dynamics control cell–basement membrane interaction in EMT during gastrulation. *Nat. Cell Biol.* **10**, 765–775 (2008).

8. O. Voiculescu, L. Bodenstein, I.-J. Lau, C. D. Stern, Local cell interactions and self-amplifying individual cell ingression drive amniote gastrulation. *eLife* **3**, e01817 (2014).

9. L. Gräper, Die Primitiventwicklung des Hühnchens nach stereokinematographischen Untersuchungen, kontrolliert durch vitale Farbmarkierung und verglichen mit der Entwicklung anderer Wirbeltiere. *Wilhelm Roux Arch. Entwickl. Mech. Org.* **116**, 382–429 (1929).

10. M. Chuai, W. Zeng, X. Yang, V. Boychenko, J. A. Glazier, C. J. Weijer, Cell movement during chick primitive streak formation. *Dev. Biol.* **296**, 137–149 (2006).

11. M. Durande, S. Tlili, T. Homan, B. Guirao, F. Graner, H. Delanoë-Ayari, Fast determination of coarse-grained cell anisotropy and size in epithelial tissue images using Fourier transform. *Phys. Rev. E* **99**, 062401 (2019).

12. C. Bertet, L. Sulak, T. Lecuit, Myosin-dependent junction remodelling controls planar cell intercalation and axis elongation. *Nature* **429**, 667–671 (2004).

13. J. T. Blankenship, S. T. Backovic, J. S. Sanny, O. Weitz, J. A. Zallen, Multicellular rosette formation links planar cell polarity to tissue morphogenesis. *Dev. Cell* **11**, 459–470 (2006).

14. J. A. Zallen, E. Wieschaus, Patterned gene expression directs bipolar planar polarity in drosophila. *Dev. Cell* **6**, 343–355 (2004).

15. J. Lavalou, Q. Mao, S. Harmansa, S. Kerridge, A. C. Lellouch, J.-M. Philippe, S. Audebert, L. Camoin, T. Lecuit, Formation of polarized contractile interfaces by self-organized Toll-8/Cirl GPCR asymmetry. *Dev. Cell* **56**, 1574–1588 (2021).

16. A. Munjal, J.-M. Philippe, E. Munro, T. Lecuit, A self-organized biomechanical network drives shape changes during tissue morphogenesis. *Nature* **524**, 351–355 (2015).

17. M. Rauzi, U. Krzic, T. E. Saunders, M. Krajnc, P. Ziherl, L. Hufnagel, M. Leptin, Embryo-scale tissue mechanics during Drosophila gastrulation movements. *Nat. Commun.* **6**, 8677 (2015).

18. S. J. Streichan, M. F. Lefebvre, N. Noll, E. F. Wieschaus, B. I. Shraiman, Global morphogenetic flow is accurately predicted by the spatial distribution of myosin motors. *eLife* **7**, e27454 (2018).

19. A. Bailles, C. Collinet, J. M. Philippe, P. F. Lenne, E. Munro, T. Lecuit, Genetic induction and mechanochemical propagation of a morphogenetic wave. *Nature* **572**, 467–473 (2019).

20. F. J. Vernerey, U. Akalp, Role of catch bonds in actomyosin mechanics and cell mechanosensitivity. *Phys. Rev. E* **94**, 012403 (2016).

21. R. Fernandez-Gonzalez, S. de Matos Simoes, J.-C. Röper, S. Eaton, J. A. Zallen, Myosin II dynamics are regulated by tension in intercalating cells. *Dev. Cell* **17**, 736–743 (2009).

22. J. M. Laakso, J. H. Lewis, H. Shuman, E. M. Ostap, Myosin I can act as a molecular force sensor. *Science* **321**, 133–136 (2008).

23. C. Veigel, J. E. Molloy, S. Schmitz, J. Kendrick-Jones, Load-dependent kinetics of force production by smooth muscle myosin measured with optical tweezers. *Nat. Cell Biol.* **5**, 980–986 (2003).

24. W. E. Thomas, V. Vogel, E. Sokurenko, Biophysics of catch bonds. *Annu. Rev. Biophys.* **37**, 399–416 (2008).

25. M. C. Marchetti, J. F. Joanny, S. Ramaswamy, T. B. Liverpool, J. Prost, M. Rao, R. A. Simha, Hydrodynamics of soft active matter. *Rev. Mod. Phys.* **85**, 1143–1189 (2013).

26. F. Graner, J. A. Glazier, Simulation of biological cell sorting using a two-dimensional extended Potts model. *Phys. Rev. Lett.* **69**, 2013–2016 (1992).

27. A. G. Fletcher, M. Osterfield, R. E. Baker, S. Y. Shvartsman, Vertex models of epithelial morphogenesis. *Biophys. J.* **106**, 2291–2304 (2014).

28. S. Alt, P. Ganguly, G. Salbreux, Vertex models: From cell mechanics to tissue morphogenesis. *Philos. Trans. R. Soc. Lond. B Biol. Sci.* **372**, 20150520 (2017).

29. A. Bonfanti, J. L. Kaplan, G. Charras, A. Kabla, Fractional viscoelastic models for power-law materials. *Soft Matter* **16**, 6002–6020 (2020).

30. R. Alert, X. Trepat, Physical models of collective cell migration. *Annu. Rev. Condens. Matter Phys.* **11**, 77–101 (2020).

31. C. Collinet, T. Lecuit, Programmed and self-organized flow of information during morphogenesis. *Nat. Rev. Mol. Cell Biol.* **22**, 245–265 (2021).

32. Y. Maroudas-Sacks, K. Keren, Mechanical patterning in animal morphogenesis. *Annu. Rev. Cell Dev. Biol.* **37**, 469–493 (2021).

33. B. Ladoux, R.-M. Mège, Mechanobiology of collective cell behaviours. *Nat. Rev. Mol. Cell Biol.* **18**, 743–757 (2017).

34. R. Etournay, M. Popović, M. Merkel, A. Nandi, C. Blasse, B. Aigouy, H. Brandl, G. Myers, G. Salbreux, F. Jülicher, S. Eaton, Interplay of cell dynamics and epithelial tension during morphogenesis of the Drosophila pupal wing. *eLife* **4**, e07090 (2015).

35. H. J. Gustafson, N. Claussen, S. De Renzis, S. J. Streichan, Patterned mechanical feedback establishes a global myosin gradient. *Nat. Commun.* **13**, 7050 (2022).

36. N. A. Dye, M. Popović, K. V. Iyer, J. F. Fuhrmann, R. Piscitello-Gómez, S. Eaton, F. Jülicher, Self-organized patterning of cell morphology via mechanosensitive feedback. *eLife* **10**, e57964 (2021).

37. N. Noll, M. Mani, I. Heemskerk, S. J. Streichan, B. I. Shraiman, Active tension network model suggests an exotic mechanical state realized in epithelial tissues. *Nat. Phys.* **13**, 1221–1226 (2017).

38. A.-C. Reymann, F. Staniscia, A. Erzberger, G. Salbreux, S. W. Grill, Cortical flow aligns actin filaments to form a furrow. *eLife* **5**, e17807 (2016).

39. E. W. Gehrels, B. Chakrabortty, M.-E. Perrin, M. Merkel, T. Lecuit, Curvature gradient drives polarized tissue flow in the *Drosophila* embryo. *Proc. Natl. Acad. Sci. U.S.A.* **120**, e2214205120 (2023).

40. A. Ioratim-Uba, T. B. Liverpool, S. Henkes, Mechano-chemical active feedback generates convergence extension in epithelial tissue. arXiv:2303.02109 (2023). https://doi.org/10.48550/arXiv.2303.02109.

41. M. Valet, E. D. Siggia, A. H. Brivanlou, Mechanical regulation of early vertebrate embryogenesis. *Nat. Rev. Mol. Cell Biol.* **23**, 169–184 (2021).

42. G. Jeffery, The motion of ellipsoidal particles immersed in a viscous fluid. *Proc. R. Soc. Lond.* **102**, 161–179 (1922).

43. C. Truesdell, W. Noll, *The Non-Linear Field Theories of Mechanics* (Springer, 2004).

44. M. Serra, S. Streichan, M. Chuai, C. J. Weijer, L. Mahadevan, Dynamic morphoskeletons in development. *Proc. Natl. Acad. Sci. U. S. A.* **117**, 11444–11449 (2020).

45. G. S. Nájera, C. J. Weijer, The evolution of gastrulation morphologies. *Development* **150**, dev200885 (2023).

46. P. Caldarelli, A. Chamolly, O. Alegria-Prévot, J. Gros, F. Corson, Self-organized tissue mechanics underlie embryonic regulation. bioRxiv 2021.10.08.463661 (2021). https://doi.org/10.1101/2021.10.08.463661.

47. R. Feroze, J. H. Shawky, M. von Dassow, L. A. Davidson, Mechanics of blastopore closure during amphibian gastrulation. *Dev. Biol.* **398**, 57–67 (2015).

48. D. R. Shook, E. M. Kasprowicz, L. A. Davidson, R. Keller, Large, long range tensile forces drive convergence during Xenopus blastopore closure and body axis elongation. *eLife* **7**, e26944 (2018).

49. M. Valet, E. D. Siggia, A. H. Brivanlou, Mechanical regulation of early vertebrate embryogenesis. *Nat. Rev. Mol. Cell Biol.* **23**, 169–184 (2022).

50. A. Carmany-Rampey, A. F. Schier, Single-cell internalization during zebrafish gastrulation. *Curr. Biol.* **11**, 1261–1265 (2001).

51. S. F. G. Krens, J. H. Veldhuis, V. Barone, D. Čapek, J.-L. Maître, G. W. Brodland, C.-P. Heisenberg, Interstitial fluid osmolarity modulates the action of differential tissue surface tension in progenitor cell segregation during gastrulation. *Development* **144**, 1798–1806 (2017).

52. R. Fernandez-Gonzalez, S. de Matos Simoes, J.-C. Röper, S. Eaton, J. A. Zallen, Myosin II dynamics are regulated by tension in intercalating cells. *Dev. Cell* **17**, 736–743 (2009).

53. R. Clément, B. Dehapiot, C. Collinet, T. Lecuit, P.-F. Lenne, Viscoelastic dissipation stabilizes cell shape changes during tissue morphogenesis. *Curr. Biol.* **27**, 3132–3142.e4 (2017).

54. V. Ferro, M. Chuai, D. McGloin, C. J. Weijer, Measurement of junctional tension in epithelial cells at the onset of primitive streak formation in the chick embryo via non-destructive optical manipulation. *Development* **147**, dev175109 (2020).

55. M. F. Staddon, K. E. Cavanaugh, E. M. Munro, M. L. Gardel, S. Banerjee, Mechanosensitive junction remodeling promotes robust epithelial morphogenesis. *Biophys. J.* **117**, 1739–1750 (2019).

56. T. Chung, *Computational Fluid Dynamics* (Cambridge Univ. Press, 2012).

57. J. S. Bois, F. Jülicher, S. W. Grill, Pattern formation in active fluids. *Phys. Rev. Lett.* **106**, 028103 (2011).

58. R. Sknepnek, I. Djafer-Cherif, M. Chuai, C. Weijer, S. Henkes, Generating active T1 transitions through mechanochemical feedback. *eLife* **12**, e79862 (2023).

59. G. Haller, Lagrangian coherent structures. *Annu. Rev. Fluid. Mech.* **47**, 137–162 (2015).

60. C. Cui, X. Yang, M. Chuai, J. A. Glazier, C. J. Weijer, Analysis of tissue flow patterns during primitive streak formation in the chick embryo. *Dev. Biol.* **284**, 37–47 (2005).

61. J. Firmino, D. Rocancourt, M. Saadaoui, C. Moreau, J. Gros, Cell division drives epithelial cell rearrangements during gastrulation in chick. *Dev. Cell* **36**, 249–261 (2016).

62. J. Ranft, M. Basan, J. Elgeti, J. F. Joanny, J. Prost, F. Jülicher, Fluidization of tissues by cell division and apoptosis. *Proc. Natl. Acad. Sci. U. S. A.* **107**, 20863–20868 (2010).

63. S. B. Shah, I. Skromne, C. R. Hume, D. S. Kessler, K. J. Lee, C. D. Stern, J. Dodd, Misexpression of chick Vg1 in the marginal zone induces primitive streak formation. *Development* **124**, 5127–5138 (1997).

Acknowledgments

Science Advances

A mechanochemical model recapitulates distinct vertebrate gastrulation modes

Mattia Serra, Guillermo Serrano Nájera, Manli Chuai, Alex M. Plum, Sreejith Santhosh, Vamsi Spandan, Cornelis J. Weijer, and L. Mahadevan

View the article online
https://www.science.org/doi/10.1126/sciadv.adh8152
Permissions
https://www.science.org/help/reprints-and-permissions

The PDF file includes:

Other Supplementary Material for this manuscript includes the following:

1 Mathematical Model

We derive our model in Cartesian coordinates and then provide an equivalent reformulation in polar coordinates.

1.1 Momentum Balance and Continuity Equation

We denote the tissue velocity field $\mathbf{v}(\mathbf{x}, t) = [u(\mathbf{x}, t), v(\mathbf{x}, t)]^\top$ and its vorticity scalar by $\omega(\mathbf{x}, t)$. We recall the velocity gradient decomposition

$$\nabla \mathbf{v}(\mathbf{x}, t) = \mathbf{S}(\mathbf{x}, t) + \mathbf{W}(\mathbf{x}, t), \tag{S1}$$

with the rate-of-strain tensor $\mathbf{S}$ and the spin tensor $\mathbf{W}$ defined as

$$\mathbf{S} = \frac{1}{2}(\nabla \mathbf{v} + \nabla \mathbf{v}^\top), \quad \mathbf{W} = \frac{1}{2}(\nabla \mathbf{v} - \nabla \mathbf{v}^\top) \equiv \frac{\omega}{2}\mathbf{R}, \quad \mathbf{R} := \begin{pmatrix} 0 & -1 \\ 1 & 0 \end{pmatrix}. \tag{S2}$$

We further decompose $\mathbf{S}$ into its isotropic and deviatoric parts as

$$\mathbf{S_s} = \mathbf{S} - \mathbf{S}_I, \quad \mathbf{S}_I = \mathbf{I}\frac{1}{2}\nabla \cdot \mathbf{v}. \tag{S3}$$

The viscous, active, total stresses and total stress trace are

$$
\begin{aligned}
\sigma_V &= -p\mathbf{I} + 2\mu \mathbf{S}_s \\
\sigma_A &= m(\mathbf{x}, t)[\mathbf{e}(\mathbf{x}, t) \otimes \mathbf{e}(\mathbf{x}, t) - \tfrac{1}{2}\mathbf{I}], \quad \mathbf{e}(\mathbf{x}, t) = [\cos \phi(\mathbf{x}, t), \sin \phi(\mathbf{x}, t)]^\top \\
\sigma_T &= \sigma_V + \sigma_A \\
\mathrm{Tr}[\sigma_T] &= -2p,
\end{aligned} \tag{S4}
$$

where μ denotes the shear viscosity, m denotes the active stress intensity arising from active myosin and ϕ the orientation of the myosin cables with respect to the $x-$axis. The friction exerted by the surrounding fluid on the epiblast is assumed to be very small, therefore we ignore substrate friction in our model.

Because viscosity is high ($\mu \approx 9 \times 10^3 \; Pa \cdot s$), we ignore inertial terms and write the momentum balance as

$$
\begin{aligned}
\nabla \cdot \sigma_T =& \nabla \cdot \sigma_V + \nabla \cdot \sigma_A = \mathbf{0} \\
\nabla \cdot \sigma_V =& \left[\begin{array}{c} -p_x \\ -p_y \end{array} \right] + \mu \left[\begin{array}{c} u_{yy} + u_{xx} \\ v_{xx} + v_{yy} \end{array} \right] \\
\nabla \cdot \sigma_A =& \frac{1}{2} \left[\begin{array}{c} \cos 2\phi \, (2m\phi_y + m_x) + \sin 2\phi(m_y - 2m\phi_x) \\ \sin 2\phi \, (2m\phi_y + m_x) - \cos 2\phi(m_y - 2m\phi_x) \end{array} \right] \\
\implies \left[\begin{array}{c} p_x \\ p_y \end{array} \right] =& \mu \left[\begin{array}{c} u_{yy} + u_{xx} \\ v_{xx} + v_{yy} \end{array} \right] + \frac{1}{2} \left[\begin{array}{c} \cos 2\phi \, (2m\phi_y + m_x) + \sin 2\phi(m_y - 2m\phi_x) \\ \sin 2\phi \, (2m\phi_y + m_x) - \cos 2\phi(m_y - 2m\phi_x) \end{array} \right].
\end{aligned}
\tag{S5}
$$

To close the system, we choose a simple continuity equation in which the flow divergence is proportional to the isotropic total stress (eq. (S4)) and active myosin concentration i.e.

$$
\begin{aligned}
\nabla \cdot \mathbf{v} =& c(\mathrm{Tr}[\sigma_T] - p_0 m) = c(-2p - p_0 m) \\
\implies p =& -\frac{\nabla \cdot \mathbf{v}}{2c} - \frac{p_0 m}{2},
\end{aligned}
\tag{S6}
$$

where c has units $[\, Pa \cdot s]^{-1}$ and p_0 is a non-dimensional parameter modulating the contribution of active myosin to flow divergence. The intuition behind eq. (S6) is that regions of high isotropic compressive stress and high active myosin, inducing isotropic apical cell contraction, exhibit negative flow divergence, i.e., cell ingression or folding. The above relation then serves as a means of writing the local pressure in terms of the flow divergence and the active myosin concentration. Equation (S6) can also be derived considering the continuity equation of a two-dimensional confluent epithelium and using the above phenomenological arguments to express the source/sink terms as a function of $\nabla \cdot \mathbf{v}$ and m. Substituting eq. (S6) into eq. (S5), we obtain the resulting force balance equations describing our active continuum without pressure terms

$$
\begin{aligned}
0 =& u_{xx}\frac{1 + 2\mu c}{2c} + u_{yy}\mu + \frac{v_{xy}}{2c} + \frac{p_0 m_x}{2} + \frac{1}{2}(\cos 2\phi \, (2m\phi_y + m_x) + \sin 2\phi(m_y - 2m\phi_x)) \\
0 =& v_{xx}\mu + v_{yy}\frac{1 + 2\mu c}{2c} + \frac{u_{xy}}{2c} + \frac{p_0 m_y}{2} + \frac{1}{2}(\sin 2\phi \, (2m\phi_y + m_x) - \cos 2\phi(m_y - 2m\phi_x)).
\end{aligned}
\tag{S7}
$$

1.2   Active Stress Orientation

We assume the evolution of actomyosin cables orientation satisfies Jeffery's equation (*42*)

$$
\phi_t = -[\mathbf{v} \cdot \nabla]\phi + \tfrac{\omega}{2} + \lambda(S_{12}\cos 2\phi + \tfrac{S_{22} - S_{11}}{2}\sin 2\phi),
\tag{S8}
$$

which describes the direction evolution of axis-symmetric fibers under a low Reynold's number flow. In eq. (S8), $\phi_t = \frac{\partial \phi}{\partial t}$, λ is a parameter quantifying the sensitivity of actomyosin cables reorientation due to shear-induced rotations, S_{ij} denotes the entries of $\mathbf{S}$ and the first two terms represent the advection term and the rigid-body rotation rate described by half of the flow vorticity.

1.3   Active Stress Magnitude

The dynamics of active myosin on actin filaments is characterized by catch bonds (*23*), i.e., the dissociation rate of actomyosin bonds depends on the tension along the actomyosin cable T_c, and decreases exponentially for increasing tension. Laser ablation experiments demonstrate that supracellular actomyosin cables exhibit higher tension and higher levels of myosin than isolated cell junctions (*52*). We explain below our reasoning to estimate T_c.

1.3.1 Junction-level modeling

Junction-level modeling of the feedback between total tension and active stress intensity supports active stress intensity as a good proxy for cable tension. Optical manipulation of apical cell-cell junctions in drosophila and chick embryo suggest that junctions are viscoelastic (*53, 54*). Among simple viscoelastic models, measurements of junction deformation through time in chick embryos are best fit by a simple Maxwell model consisting of a spring and dashpot in series (*54*) (Figure S1A). Thus, we consider each junction as a Maxwell element in parallel with an active element generating additional active stresses (Figure S1B). Maxwellian viscoelasticity has been frequently used to model single-junction dynamics in drosophila (*35, 37, 53*). It is easy to show that the tension of a Maxwell element can be written as an elastic term with a continuously relaxing rest length (*55*). Consistent with the assumption of Maxwellian viscoelasticity and additional tension induced by myosin activity, the total junction tension is

$$T_{ij} = K(r_{ij} - l_{ij}) + m_{ij}, \tag{S9}$$

where K is a spring constant, $r_{ij} = r_j - r_i$ is the length between vertex positions, l_{ij} is a dynamic rest length at which elastic tension vanishes, and m_{ij} represents an active stress intensity due to myosin activity. The rest length relaxes to the junction length over time as

$$\frac{dl_{ij}}{dt} = (r_{ij} - l_{ij}) \frac{1}{\tau}, \tag{S10}$$

where τ is the relaxation time. We model the dynamics of myosin activity (active stress intensity) in terms of mechanisms for myosin recruitment and tension-dependent dissociation

$$\frac{dm_{ij}}{dt} = \left(\frac{m_n}{t_r} - \frac{m_{ij}}{t_d} e^{-k_o T_{ij}} - \chi m_{ij} \right) \frac{t_p}{t_c}, \tag{S11}$$

where t_r is the recruitment time scale of myosin from the cytoplasm, which has a given maximum concentration m_n, and $t_d^{-1} e^{-k_o T_{ij}}$ represents the tension-dependent dissociation rate of actomyosin cables. χ has units $[t^{-1}]$ and accounts for the saturation of myosin activity on junctions, ensuring that active stress cannot accumulate without bound. Physically, available myosin may be depleted from basal pools or the number of active myosin motors that can operate on actin filaments may be limited. In this work, we remain agnostic as to which saturation mechanisms may operate and their relative contributions, so we capture saturation effects with a simple linear term. Later, we show that our results are not sensitive to the saturation mechanism. Note again that m, m_n have units $[Pa]$ as they describe the stress magnitude arising from active myosin. From the time when active myosin is available to the time it generates active stresses, there is a time scale (t_p). We model this delay with the ratio (t_p/t_c), where t_c is the characteristic time scale of the system.

Equations (S9-S11) model the coupled dynamics of tension and myosin activity in a single junction (Figure S1B). To couple the dynamics of adjacent edges and model a supracellular actomyosin cable, we further assume relaxational vertex dynamics. Restricting the cable to one dimension, the dynamics of each vertex are dominated by its two neighboring cable edges as

$$\frac{dr_i}{dt} = \frac{1}{\nu} \left(T_{i,i+1} - T_{i,i-1} \right), \tag{S12}$$

where ν represents effective friction resisting vertex displacement (*37, 35, 53*). The effective friction models the internal dissipative mechanisms such as the interaction of the cell junction with the cytosol and the viscous flow induced in the cytoskeleton due to the motion of the cell vertices (*28*). External dissipation by the surrounding fluid is assumed to be minimal. Thus, the length r_{ij} between vertices experiences a strain rate

$$\frac{dr_{ij}}{dt} = \frac{dr_j}{dt} - \frac{dr_i}{dt} = \frac{1}{\nu} \left(T_{i,j+1} - T_{i,j} - T_{i,j} + T_{i-1,i} \right) = \frac{\Delta T_{ij}}{\nu}, \tag{S13}$$

where Δ is the discrete Laplacian. In the continuum limit, we replace the discrete laplacian with $\Delta \bar{l}^2$, where $\bar{l}$ is the characteristic junction length (*37*). This provides two coupled equations for the dynamics of tension and myosin

activity:

$$\begin{cases} \frac{\partial T}{\partial t} = \frac{K\bar{l}^2}{\nu}\Delta T - \frac{T-m}{\tau} + \left(\frac{m_n}{t_r} - \frac{m}{t_d}e^{-k_o T} - \chi m\right)\frac{t_p}{t_c} \\ \frac{\partial m}{\partial t} = \left(\frac{m_n}{t_r} - \frac{m}{t_d}e^{-k_o T} - \chi m\right)\frac{t_p}{t_c}. \end{cases} \tag{S14}$$

These equations can be combined to give a differential equation for the difference between T and m

$$\frac{\partial(T-m)}{\partial t} = \frac{K\bar{l}^2}{\nu}\Delta T - \frac{T-m}{\tau}, \tag{S15}$$

which can also be understood as a differential equation for the elastic (or passive) component of the tension. The first term causes elastic tension to propagate along cables. The second term causes elastic tension to diminish as the rest length relaxes. Where the propagation term dominates, we expect transient deviations between m and T. Otherwise, the dynamics tend to reach $T = m$. Simulating equations (S14) with an initial central peak of active stress intensity, we find that, when $\frac{K\bar{l}^2\tau}{\nu}$ is small, T and m follow one another closely, as shown in Movie S13 and Figure S1C.
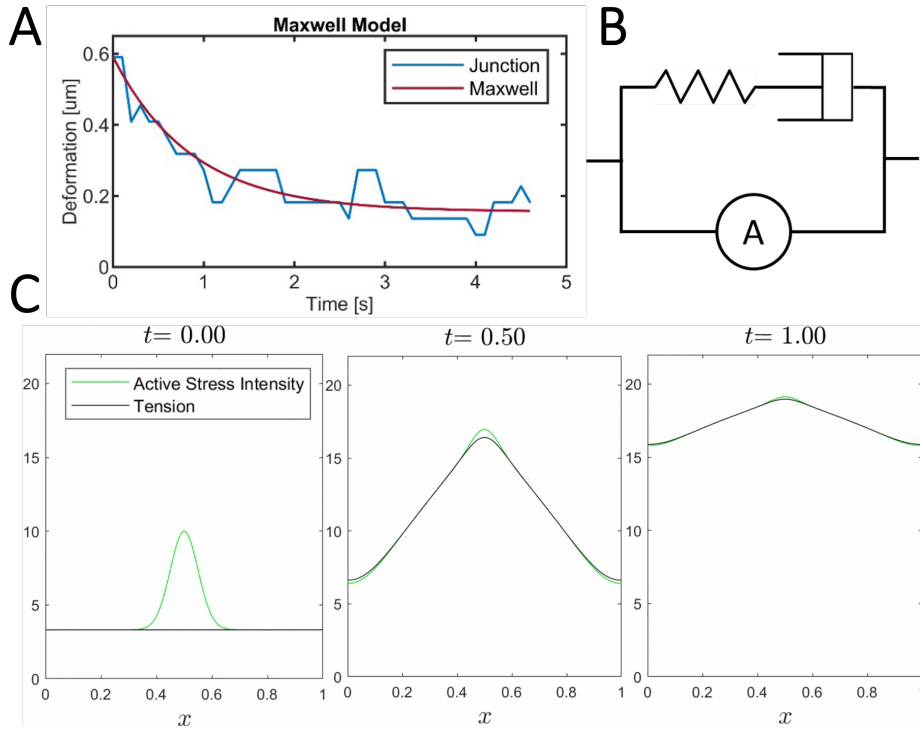
Supplementary Figure S1: **Mechanical feedback along a 1D cable.** A) Chick embryo experimental data from (*54*) shows that a junction deformed through optical manipulation exhibits a response that is best fit by Maxwellian viscoelasticity. B) Mechanical element for an actomyosin cable, consisting of a Maxwell element in parallel with an active element. C) Plots from the evolution of (S14) for sample parameters $\frac{K\bar{l}^2}{\nu} = 1$, $\tau = 0.001$, and $\chi\frac{t_p}{t_c} = 2.5$ so that cable tension reaches a maximum of $m = T = 20$. Sample parameters: $\frac{m_n t_p}{t_r t_c} = 50$, $\frac{t_p}{t_d t_c} = 100$, $k_o = 0.625$, $dx = 0.01$, $dt = 0.00001$.

1.3.2 Tissue-level modeling and time scales

The tissue-scale behavior is fluid-like and hence well described by viscous and active stresses (eq.(S5)) at gastrulation time scales. Extending the above reasoning to the tissue scale, active myosin contributes to cable tension T_c through an active stress contribution $T_A = \langle\mathbf{e}, \sigma_A\mathbf{e}\rangle = \frac{m}{2}$. At the junction level, T_A corresponds to m_{ij}, leaving $K(r_{ij} - l_{ij})$ to be accounted for. One can also compute from the viscous stress $T_V = \langle\mathbf{e}, \sigma_V\mathbf{e}\rangle$. However, σ_V and T_V reflect

fluid-like tissue stresses arising from cell division and intercalation. If and how T_V may affect junction-level cable tension is unclear. Regardless, we expect this effect to be of secondary importance because myosin-induced (active) tension (T_A) dominates T_V (*37*).

We are not aware of estimates for K or ν, so we cannot precisely estimate $\frac{K\bar{l}^2}{\nu}$. Moreover, the junction-level modeling presumes propagation over a 1D cable with no constraints on its extent. In the tissue, however, super-cellular cables have a limited extent spanning from 2 to 8 cells (*5*). Therefore, even if K and ν were known, propagation strength should be reduced by the effective length of super-cellular cables, which is small compared to the tissue scale. Last, the junction relaxation time has been estimated to be in the order of seconds in the chick epiblast (*54*). Altogether, the fast relaxation of the junction rest length and a small $\frac{K\bar{l}^2}{\nu}$ suggests that the elastic component of the tension is negligible at leading order. Following brief periods of rest length relaxation, mechanical feedback adjusts myosin activity to balance the tension of neighboring junctions (*35*). This is consistent with experimental observations that levels of myosin activity can serve as a readout for tension on cell junctions (*2*). Thus, in our coarse-grained continuum model, which neglects short-timescale elasticity and considers longer timescales over which the epithelium is effectively viscous, we expect

$$T_c \approx T_A = \tfrac{m}{2}, \tag{S16}$$

and that m will exhibit some effective propagation of active stress intensity along cables in their predominant orientation ϕ. In two dimensions, the effects of this directional propagation can be captured by two directional derivatives along the cable, $\Delta_\phi = D_\phi D_\phi$, and with a coefficient ξ modulating the tissue-scale effect of tension propagation. The definition $\Delta_\phi = D_\phi D_\phi$ is a simplification of the more general $(\mathbf{e} \cdot \nabla)^2$ and assumes that the individual cables along which propagation occurs are approximately straight locally.

We reason that at the tissue scale, the dynamics of active stress intensity are governed by similar mechanisms of myosin recruitment and tension-dependent dissociation modeled at the junction scale. Using the above assumptions and eq. (S16), we model the evolution of active stress magnitude as

$$m_t = (\tfrac{m_n}{t_r} - e^{-k_o \frac{m}{2}} \tfrac{m}{t_d} - \chi m)\tfrac{t_p}{t_c} - [\mathbf{v} \cdot \nabla]m + \xi \Delta_\phi m. \tag{S17}$$

The last two terms account for the advection of active stress intensity through material transport of actomyosin cables and for the directed propagation of active stress intensity along actomyosin cables with Δ_ϕ defined as the second directional derivative along the cable direction ϕ.

1.4   Model in Cartesian coordinates

The full model describing our active continuum can be summarized as

$$
\begin{cases}
\mathbf{0} = & u_{xx}\tfrac{1+2\mu c}{2c} + u_{yy}\mu + \tfrac{v_{xy}}{2c} + \tfrac{p_0 m_x}{2} + \tfrac{1}{2}(\cos 2\phi\, (2m\phi_y + m_x) + \sin 2\phi(m_y - 2m\phi_x)) \\
& v_{xx}\mu + v_{yy}\tfrac{1+2\mu c}{2c} + \tfrac{u_{xy}}{2c} + \tfrac{p_0 m_y}{2} + \tfrac{1}{2}(\sin 2\phi\, (2m\phi_y + m_x) - \cos 2\phi(m_y - 2m\phi_x)) \\
\phi_t = & \lambda(\tfrac{u_y + v_x}{2}\cos 2\phi + \tfrac{v_y - u_x}{2}\sin 2\phi) - [\mathbf{v} \cdot \nabla] + \tfrac{\omega}{2} \\
m_t = & (\tfrac{m_n}{t_r} - e^{-k_o \frac{m}{2}}\tfrac{m}{t_d} - \chi m)\tfrac{t_p}{t_c} - [\mathbf{v} \cdot \nabla]m + \xi\Delta_\phi m \\
& + \text{Boundary Conditions and Initial Conditions.}
\end{cases} \tag{S18}
$$

1.4.1 Non-dimensional model in Cartesian coordinates

Denoting by $u_c, x_c, t_c = x_c/u_c$ and $m_c = \mu u_c/x_c$ the characteristic velocity, characteristic length scale, characteristic time scale and the characteristic viscous shear stress, we rewrite eq. (S18) in non-dimensional compact form as

$$
\begin{cases}
0 = & 2p_1\Delta\mathbf{v} + \nabla[\nabla\cdot\mathbf{v}] + 2p_1\mathbf{B}\nabla m + p_1(p_0-1)\nabla m + 2p_1\nabla\cdot\mathbf{B}m \\
\phi_t = & \frac{p_2}{2}[\sin 2\phi(v_y - u_x) + \cos 2\phi(u_y + v_x)] - [\mathbf{v}\cdot\nabla]\phi + \frac{\omega}{2} \\
m_t = & p_3 - p_4 e^{-\frac{p_5}{2}m}m - p_6 m - [\mathbf{v}\cdot\nabla]m + p_7\Delta_\phi m \\
& + \text{Boundary Conditions and Initial Conditions},
\end{cases}
\tag{S19}
$$

where

$$
\mathbf{B} = \mathbf{e}\otimes\mathbf{e} = \begin{pmatrix} \cos^2\phi & \sin\phi\cos\phi \\ \sin\phi\cos\phi & \sin^2\phi \end{pmatrix},
$$

and m, ϕ, u, v, x, y, t are nondimensional. In eq. (S19), there are seven nondimensional parameters

$$
p_0, \quad p_1 = \mu c, \quad p_2 = \lambda, \quad p_3 = \frac{t_p}{t_r}\frac{m_n}{m_c}, \quad p_4 = \frac{t_p}{t_d}, \quad p_5 = \frac{k_o\mu u_c}{x_c}, \quad p_6 = \chi t_p, \quad p_7 = \frac{\xi}{x_c u_c}.
\tag{S20}
$$

p_0 describes the cell's propensity of ingressing from a myosin-induced apical isotropic contraction and can be thought of also as the ratio of isotropic to anisotropic active stresses. p_1 describes the ratio of the shear to bulk viscosity, p_2 is the alignment parameter that describes how the actomyosin cables tend to orient due to shear-induced rotations and is ≈ 1 for elongated fibers. p_3 represents the ratio of the myosin (or active stress intensity) recruitment time scale t_r, from the ambient myosin pool of concentration m_n/m_c, to the characteristic t_p time scale, multiplied by m_n/m_c. p_4 represents the ratio of the t_p time scale to the dissociation time scale t_d. p_5 is the product of the characteristic viscous shear stress and k_o, which represents the inverse of the characteristic tension of the actomyosin cables (with units $[Pa]^{-1}$). p_6 is the strength of the simplest linear saturation term set by the ratio of t_p to the characteristic dissociation time scale χ^{-1} controlling saturation. Practically, p_6 enables setting a desired saturation level for m. p_7 is the ratio between transport of the active stress magnitude via tension propagation (with effective diffusion constant ξ) and active stress magnitude transport via advection.

The first two terms of the force balance are a viscous force and a force arising from compressibility inhomogeneities. Instead, the last three terms are active forces induced by m and ϕ inhomogeneities. Finally, observing the first two terms in the last equation of (S19), we note that more myosin induces higher tension on the cables, which in turn decreases the dissociation rate: $(m\uparrow) \to T_c\uparrow$ (more positive) $\to$ diss. rate $\downarrow$ $\to$ myosin increases $(m\uparrow)$ (Figure 2A). This observation suggests an instability, which will become clear in section 1.4.3.

1.4.2 Role of p_0

To gain insights on p_0, we rewrite the force balance as

$$
\nabla[\nabla\cdot\mathbf{v}] = p_1(1-p_0)\nabla m - 2p_1\mathbf{B}\nabla m - 2p_1\Delta\mathbf{v} - 2p_1 m\nabla\cdot\mathbf{B}.
\tag{S21}
$$

From eq. (S6), we know that $p_0 \geq 0$ reflects the expectation that high myosin induces isotropic apical cell contraction that causes active cell ingression. To elucidate the effect of p_0 on the relation between $\nabla[\nabla\cdot\mathbf{v}]$ and ∇m, we neglect the shear force $(-2p_1\Delta\mathbf{v})$, assume a simplified uniform ridge of active myosin in the y direction (Figure S2), and a spatially uniform cable distribution (i.e., $\nabla\cdot\mathbf{B} = 0$). Therefore, eq. (S21) simplifies to

$$
\nabla[\nabla\cdot\mathbf{v}] \approx p_1(1-p_0)\nabla m - 2p_1\mathbf{B}\nabla m.
\tag{S22}
$$

If cables are perpendicular to the myosin ridge (Figure S2A), as in the wild-type development (Figure 1E at HH3 and Figure 2C right), eq. (S22) reveals that for all $p_0 \geq 0$, ∇m and $\nabla[\nabla\cdot\mathbf{v}]$ have opposite directions, reflecting the expectation that a ridge of high myosin induces a sink in the velocity field (Figure 2H). By contrast, if cables are

parallel to the myosin ridge (Figure S2B-C) as in the case of perturbation 3 (Figure 4 of (*4*) and Movie8), eq. (S22) reveals that for all $p_0 > 1$ (Figure S2B), ∇m and $\nabla[\nabla \cdot \mathbf{v}]$ have opposite directions. On the contrary, if $p_0 < 1$, ∇m and $\nabla[\nabla \cdot \mathbf{v}]$ would have the same direction (Figure S2C). Therefore, combining our model with experimental observations, we use $p_0 > 1$ when active cell ingression is present, and $p_0 = 0$ otherwise.
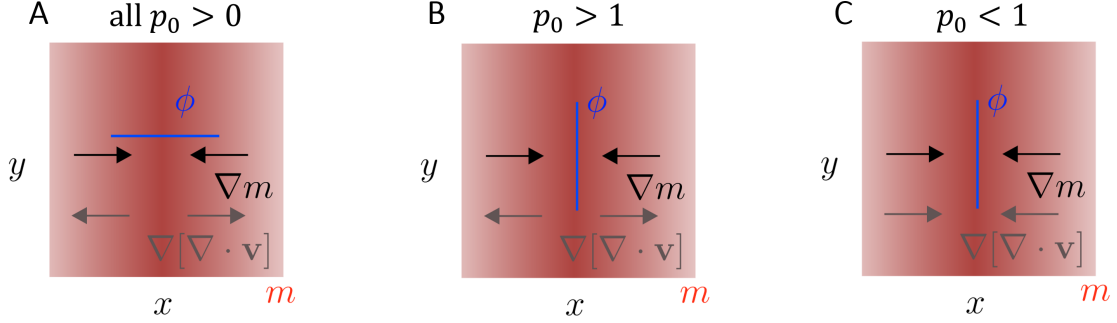
Supplementary Figure S2: **Influence of p_0 on the relationship between ∇m and $\nabla[\nabla \cdot \mathbf{v}]$.** We consider a simplified force balance (eq. (S22)) with no shear forces, a simple distribution m made of a ridge in the y direction and uniform actomyosin cables (i.e., $\nabla \cdot \mathbf{B} = \mathbf{0}$) perpendicular (A) or parallel (B, C) to the myosin ridge. Equation (S22) reveals that when cables are perpendicular (A) to the ridge, ∇m and $\nabla[\nabla \cdot \mathbf{v}]$ have opposite directions for all values of $p_0 > 0$, reflecting the expectation that a ridge of high myosin induces a sink in the velocity field. When cables are perpendicular to the ridge, ∇m and $\nabla[\nabla \cdot \mathbf{v}]$ have opposite directions for $p_0 > 1$ (B), and the same direction for $p_0 < 1$.

1.4.3 One-dimensional model

To gain insights about the model (S19), we assume slow dynamics in the $y-$direction, ignore the $\phi-$dynamics and set $\phi = 0$, obtaining the following simplified one-dimensional model

$$\begin{cases} 0 = u_{xx}(1 + 2p_1) + p_1\, m_x(1 + p_0) \\ m_t = p_3 - p_4 e^{-\frac{p_5}{2}m}m - p_6 m - m_x u + p_7 m_{xx}. \end{cases} \tag{S23}$$

Equation (S23) describes the dynamics along a straight line perpendicular to the primitive streak. We set Dirichlet boundary conditions on the velocity $u(0,t) = -|u_b|$, $u(L,t) = |u_b|$ consistent with the symmetric cell migration in the extra-embryonic area, and no-flux boundary conditions for m: $m_x(0,t) = m_x(L,t) = 0$.

We investigate the main features of eq. (S23) by seeking the constant fixed points for m which solve the implicit equation $p_3 - (p_4 e^{-\frac{p_5}{2}m} + p_6)m = 0$. From the first equation, we compute the corresponding equilibrium velocity field $u_{eq.} = \frac{2|u_b|}{L}x - |u_b|$. We then study the linear stability of these equilibrium solutions by computing the spectrum of the corresponding linearized PDE. Denoting by $\delta \mathbf{h} = [\delta u, \delta m]^\top$ the perturbation from the equilibrium, we compute the linearized version of Eq. (S23) in operator form as $\mathcal{A}\delta\mathbf{h} = \mathcal{B}(x)\delta\mathbf{h}$ where

$$\mathcal{A} = \begin{bmatrix} 0 & 0 \\ 0 & \partial_t \end{bmatrix}, \; \mathcal{B}(x) = \begin{bmatrix} (1 + 2p_1)\partial_{xx} & p_1(1 + p_0)\partial_x \\ 0 & \frac{1}{2}e^{-\frac{1}{2}p_5 m_{eq.}}p_4(p_5 m_{eq.} - 2) - (\frac{2|u_b|}{L}x - |u_b|)\partial_x - p_6 + p_7\partial_{xx} \end{bmatrix}, \tag{S24}$$

whose boundary conditions are inherited from the nonlinear problem, and correspond to zero Dirichlet boundary conditions for δu and zero flux boundary conditions for δm. We discretize the linearized PDE using a centered finite differencing scheme (*56*) and compute the generalized eigenvalue problem associated with eq. (S24).
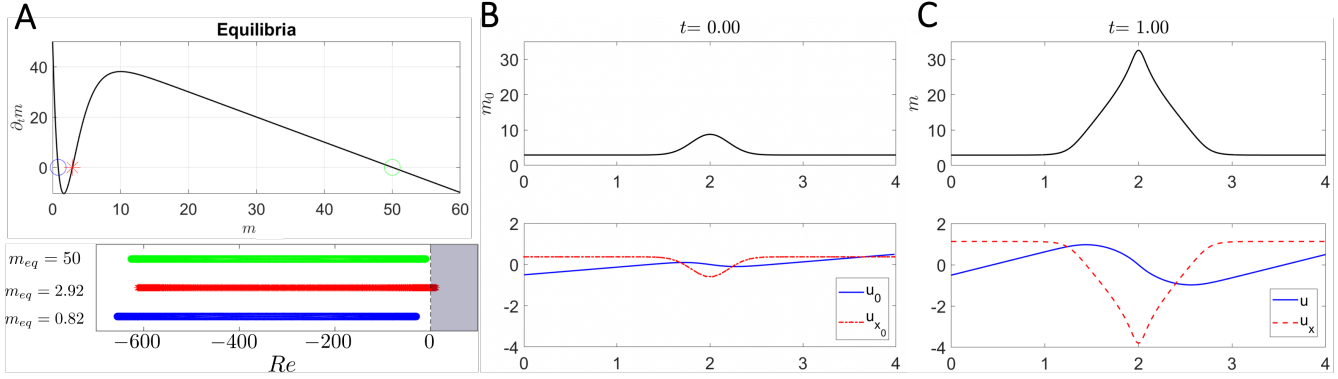
Supplementary Figure S3: **1D model**. (A) Top: Graph of $p_3 - (p_4 e^{-\frac{p_5}{2}m} + p_6)m = 0$ shows three $m_{eq.}$ marked with a blue circle, a red asterisk, and a green circle. Bottom: Truncated spectrum of the linearized PDE around corresponding $m_{eq.}$, $u_{eq.}$, consisting of the 500 eigenvalues with the highest real part. The spectrum at the intermediate equilibrium has positive real parts, implying that the intermediate equilibrium is linearly unstable. (B) The initial condition of the nonlinear 1D model using as initial myosin concentration a Gaussian added to the higher unstable $m_{eq.}$. The blue curve shows the associated initial velocity u_0, and the red dashed curve the initial velocity divergence u_{x_0}. (C) Same as B at the final time. The full time evolution is available as Movie S1. Sample parameters: $p_0 = 2$, $p_1 = 0.25$, $p_3 = 50$, $p_4 = 100$, $p_5 = 1.25$, $p_6 = 1$, $p_7 = 0.01$, $u_b = 0.5$, $L = 4$, $dx = 0.008$, $dt = 0.0001$.

Supplementary Figure S3A top shows three equilibria $m_{eq.}$, while the bottom panel shows the corresponding 500 eigenvalues, with the largest real part, of the linearized operator. The spectrum shows that the lowest and highest equilibria are linearly stable while the intermediate equilibrium is linearly unstable for the chosen parameter values. We confirm these linearized results by solving the full nonlinear PDE from an initial Gaussian m distribution (Figure S3B) added to the unstable $m_{eq.}$ (Figure S3A top, red asterisk). From a biological perspective, a region of higher m_0 represents the mesendoderm precursor. At later times (Figure S3C), m undergoes a focusing instability, that in turn generates a 1D attractor corresponding to the PS and marked by a peak of negative divergence (red dashed curve). The complete time evolution is available as Movie S1. Finally, the velocity divergence u_x shows a contracting region close to the PS as well as two symmetric expanding regions close to the boundary, consistent with the isotropic deformations observed in the Embryonic and Extra-Embryonic territories (*2*). Our simple 1D model reproduces several key features of amniote gastrulation. Yet, it is insufficient to reproduce the convergent extension and vortical patterns observed in experiments, which we investigate with our 2D model.

We note that eq. (S23) differs from the one-dimensional isotropic active gel instability in (*57*). Despite both associated with the dynamics of actomyosin on the cell cortex, eq. (S23) models myosin exchange with the cytoplasm as opposed to (*57*), which assume no exchange with the cytoplasm (eq. (1) and [8] in (*57*)). Additionally, our model accounts for catch-bonds between actin and myosin in the form experimentally measured in (*23*), which is absent in (*57*). Finally, (*57*) accounts for friction with the substrate, absent in our case. For a more detailed biological explanation behind the myosin exchange with the cytoplasm and the catch-bond mechanism in our context, we refer the reader to Figure 3 of (*5*).

1.5 Model in polar coordinates

Because of the circular geometry of the Extra-embryonic tissue and the symmetric radial cellular motion at its outer boundary, we write model (S18) in polar coordinates.
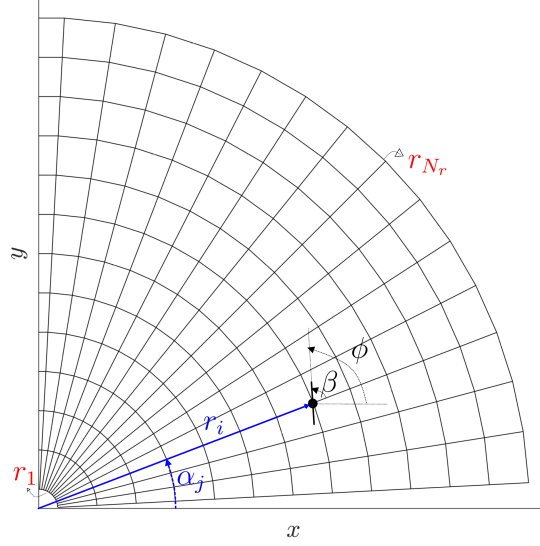
Supplementary Figure S4: **Numerical mesh.** Illustration of the discretization grid (first quadrant) used to solve eq. (S26). β denotes the cables orientation relative to α.

Denoting the velocity field by $\mathbf{v} = u(r,\alpha,t)\mathbf{e_r} + v(r,\alpha,t)\mathbf{e_\alpha}$ and the cables orientation relative to α by β (Figure S4), we obtain

$$
\begin{cases}
0 = \frac{r^2(1+2c\mu)u_{rr}+2c\mu u_{\alpha\alpha}+r(1+2c\mu)u_r-(1+2c\mu)u-(1+4c\mu)v_\alpha+rv_{r\alpha}+p_0cr^2m_r+cr\sin 2\beta[m_\alpha-2rm\beta_r]+cr\cos 2\beta[rm_r+2m(1+\beta_\alpha)]}{2cr^2} \\[4pt]
0 = \frac{2c\mu r^2v_{rr}+(1+2c\mu)v_{\alpha\alpha}+2c\mu rv_r-2c\mu v+(1+4c\mu)u_\alpha+ru_{r\alpha}+p_0crm_\alpha+cr\sin 2\beta[2m(1+\beta_\alpha)+rm_r]-cr\cos 2\beta[m_\alpha-2rm\beta_r]}{2cr^2} \\[4pt]
\beta_t = \frac{v-u_\alpha+rv_r}{2r} + \frac{\lambda}{2r}[\cos 2\beta(u_\alpha-v+rv_r)+\sin 2\beta(u+v_\alpha-ru_r)] - \left(\frac{v[1+\beta_\alpha]}{r}+u\beta_r\right) \\[4pt]
m_t = \left(\frac{m_n}{t_r}-e^{-k_o\frac{m}{2}}\frac{m}{t_d}-\chi m\right)\frac{t_p}{t_c} - \left(\frac{vm_\alpha}{r}+um_r\right) + \xi[m_{rr}\cos^2\beta + m_{\alpha\alpha}\sin^2\beta + \left(\frac{m_{\alpha r}}{r}-\frac{m_\alpha}{2r^2}\right)\sin 2\beta] \\[4pt]
u(r_{N_r},\alpha,t)=|u_b|,\ v(r_{N_r},\alpha,t)=0,\ \beta_r(r_{N_r},\alpha,t)=0,\ m_r(r_{N_r},\alpha,t)=0 \\[4pt]
+ \text{ Initial Conditions,}
\end{cases}
$$
(S25)

which, in non-dimensional form, becomes

$$
\begin{cases}
0 = (u_{rr}-\frac{u}{r^2}+\frac{u_r}{r})(\frac{1+p_1}{p_1})+\frac{u_{\alpha\alpha}}{r^2}+\frac{v_{r\alpha}}{rp_1}-\frac{v_\alpha}{r^2}(\frac{1+2p_1}{p_1})+\frac{p_0m_r}{2}+\cos 2\beta(\frac{m[1+\beta_\alpha]}{r}+\frac{m_r}{2})-\sin 2\beta(-\frac{m_\alpha}{2r}+m\beta_r) \\[4pt]
0 = v_{rr}+\frac{v_{\alpha\alpha}}{r^2}(\frac{1+p_1}{p_1})+\frac{u_{r\alpha}}{rp_1}+\frac{v_r}{r}+\frac{u_\alpha}{r^2}(\frac{1+2p_1}{p_1})-\frac{v}{r^2}+\frac{p_0m_\alpha}{2r}+\cos 2\beta(-\frac{m_\alpha}{2r}+m\beta_r)+\sin 2\beta(\frac{m[1+\beta_\alpha]}{r}+\frac{m_r}{2}) \\[4pt]
\beta_t = \frac{v-u_\alpha}{2r}+\frac{v_r}{2}+\frac{p_2}{2}[\cos 2\beta(\frac{u_\alpha-v}{r}+v_r)+\sin 2\beta(-u_r+\frac{u+v_\alpha}{r})] - \left(\frac{v[1+\beta_\alpha]}{r}+u\beta_r\right) \\[4pt]
m_t = p_3-p_4e^{-\frac{p_5}{2}m}m-p_6m-\left(\frac{vm_\alpha}{r}+um_r\right)+p_7[m_{rr}\cos^2\beta+m_{\alpha\alpha}\sin^2\beta+\left(\frac{m_{\alpha r}}{r}-\frac{m_\alpha}{2r^2}\right)\sin 2\beta] \\[4pt]
u(r_{N_r},\alpha,t)=|u_b|,\ v(r_{N_r},\alpha,t)=0,\ \beta_r(r_{N_r},\alpha,t)=0,\ m_r(r_{N_r},\alpha,t)=0 \\[4pt]
+ \text{ Initial Conditions.}
\end{cases}
$$
(S26)

2 Numerical Scheme

We develop a finite-difference numerical scheme to solve eq. (S26) in MATLAB. First, we multiply the momentum balance equations by r^2, leaving their solutions unaltered while avoiding numerical issues at grid points close to the origin. Then, we discretize spatial differential operators using centered finite-difference at second-order accuracy, except at the grid points (r_1,α_j) (Figure S4), where we use forward finite-difference at second-order accuracy (*56*).

We solve the first two equations for u, v by inverting (once) the corresponding discretized differential operator, which we multiply at each time step to the discretized forcing vector arising from the updated β, m-dependent terms. We adopt a two-step Adams–Bashforth method to solve the last two PDEs for β and α.

Because the cables orientation is a direction instead of a vector field, spatial derivatives of β need special care. Specifically, when computing $\beta_r(i,j) \approx \frac{\beta(i-1,j)-\beta(i+1,j)}{2\Delta r}$, one should make sure that both the sign and the amplitude are correct. We do so by rewriting $\frac{\beta(i-1,j)-\beta(i+1,j)}{2\Delta r} = \beta_r^p(i,j)+\beta_r^m(i,j)$, where $\beta_r^p(i,j) = \frac{\beta(i+1,j)-\beta(i,j)}{2\Delta r}$, $\beta_r^m(i,j) = \frac{\beta(i,j)-\beta(i-1,j)}{2\Delta r}$, and compute $\beta_r^p(i,j) = \text{sign}(\langle \mathbf{e}_{\beta(i+1,j)} \times \mathbf{e}_{\beta(i,j)}, \hat{\mathbf{e}}_z \rangle) \arccos \langle \mathbf{e}_{\beta(i+1,j)}, \mathbf{e}_{\beta(i,j)} \rangle$, where $\mathbf{e}_\beta = [\cos\beta, \sin\beta, 0]$, $\hat{\mathbf{e}}_z = [0,0,1]$. The same strategy can be used for higher-order derivatives and forward finite difference schemes. We summarize our numerical scheme in the following algorithm.

Algorithm 1 Numerical Solver of eq. (S26)

Inputs:

Grid: $r_i = i\Delta r$, $i = 1...N_r$, $N_r\Delta r = L$, $\alpha_j = \frac{\Delta\alpha}{2} + j\Delta\alpha$, $j = 0...N_{\alpha-1}$, $N_\alpha\Delta\alpha = 2\pi$

Initial Conditions: $m(r,\alpha,0)$, $\beta(r,\alpha,0)$

Parameters: p_i, $i = 0,..,7$

1. Solve for $u(r,\alpha,0)$, $v(r,\alpha,0)$ from the first two equations

2. Compute $m(r,\alpha,\Delta t)$, $\beta(r,\alpha,\Delta t)$ using $m(r,\alpha,0)$, $\beta(r,\alpha,0)$, $u(r,\alpha,0)$, $v(r,\alpha,0)$

3. Repeat step 1 and 2 for all $t_k = k\Delta t$, $k = 0,..,N_t$, $T_f = N_t\Delta t$

Outputs: u, v, β, m at all grid points $\{r_i, \alpha_j, t_k\}$.

To prevent the development of sharp derivatives in β at the origin due to the forward finite-difference scheme, we add a diffusion term in the β_t equation with a non-dimensional prefactor of 10^{-3}. In all our simulations, we use $\Delta r = 0.05$, $L = 1$, $\Delta\alpha = 4°$, $\Delta t = 5 \times 10^{-6}$, $T_f \approx 1$. We monitor the accuracy of our numerical solver by substituting our solution at each time step into the momentum balance equations. We find deviations from zero of the order $\approx 10^{-11}$.

3 Induction of active stress intensity via tension propagation

To visualize the effect of directed propagation (Δ_ϕ) of active tension in polar coordinates, we solve the m_t equation in (S26) activating only the diffusion term on the right-end side. Figure S5A shows the evolution of active stress intensity m starting with high values in the sickle-shaped region of mesendoderm precursors. At later times, active stress intensity propagates around the epiblast due to the tension-propagation mechanism captured by $p_7\Delta_\phi m$ (Figure S5B). In the full model, however, all terms in eq. (S17) contribute to the evolution of m. Because the tissue is fluidized, the propagation of active stress intensity is dominated by advection so that active stress intensity does not appear to spread to the full extent depicted in Figure S5.
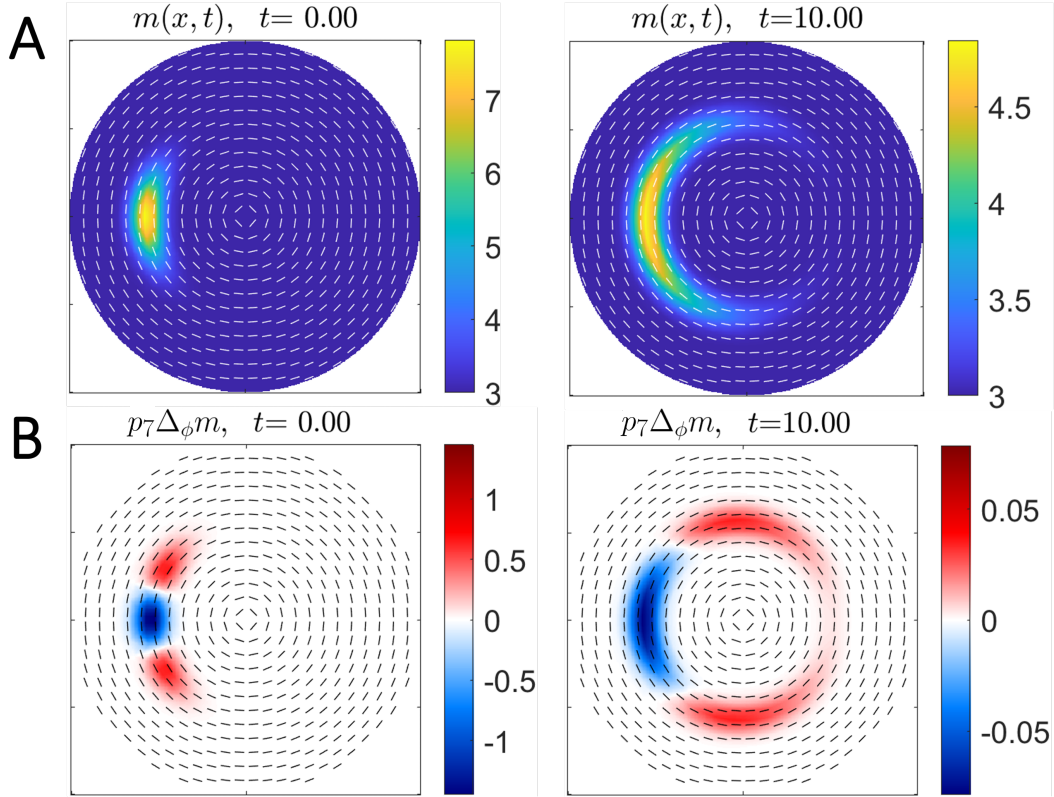
Supplementary Figure S5: **Visualization of directional propagation of active stress intensity.** A) Initial and final distribution of active stress intensity m under evolution $m_t = p_7\Delta_\phi m$ with no evolution of $\mathbf{v}$ or ϕ. B) Initial and final distribution of $p_7\Delta_\phi m$. Active stress orientations are indicated by white (A) and black (B) line segments. Sample parameter: $p_7 = 0.01$.

4 Parameters, boundary and initial conditions: selection and sensitivity analysis

In all our simulations, we use a single set of parameter values summarized in table 1.

| p_0	p_1	p_2	p_3	p_4	p_5	p_6	p_7
0 or 2	0.15	0.9	50	100	1.25	1	0.01

Table 1: Parameter values.

We have selected parameter values using a combination of experiments, mechanistic arguments and numerical simulations; and have performed sensitivity analyses with respect to parameter changes as described below.

4.1 p_0, p_1, p_2

According to our arguments in Section 1.4.2, we set $p_0 = 0$ when active cell ingression is inhibited with drugs and $p_0 = 2$ otherwise. We use $p_1 = 0.15$ and note that increasing p_1 models a more compressible tissue. With higher p_1, the typical counter-rotating vortices (polonaise movement) disappear due to increased cell ingression and less cell redistribution (see Fig.S11). From Jeffery's equation (S8), p_2 modulates the rotation rate due to shear of a material fiber, which is ≈ 1 for elongated fibers. Here we set $p_2 = 0.9$, and note that slight variations of this value does not affect our results, as shown in WT simulations Movie S14 (Movie S15) for $p_2 = 0.6$ ($p_2 = 1$).

4.2 p_3, p_4, p_5

t_p is the approximate time required to observe active stress at the tissue scale generated by active myosin cables. This phenomenon involves a complex cascade of operations from kinetic reactions to single-cell and multicellular mechanochemical processes. Here we estimate t_p using the typical time for a junction to fully contract and induce an intercalation event driven by junctional myosin, a robust and experimentally accessible readout of tissue-scale active stress induced by actomyosin cables. Experiments in the chick epiblast show that this process takes up to $\approx 20min$ (*2*). A typical time course is shown in fig 4F of (*2*) where it takes 60 minutes for three junctions to successively contract. See also supplementary videos 10 and 11 of (*2*) which show various examples of intercalating cells, where it takes 4-10 frames (1 frame is 3 minutes) for junctions to contract. This result is consistent with tissue-scale mechanochemical models, where the actomyosin or active stress dynamics is the slowest (*37, 35, 58*), and a given configuration of active stress generates the corresponding tissue-scale velocity field by solving a static force balance (eq. 1 in S19). The recruitment and dissociation time scales are $t_r \simeq t_d \approx 10$s in line with observations made in Drosophila (*53*). With these estimates, we set $p_3 = 50$ and $p_4 = 100$. p_5 is the coupling strength regulating myosin intensity and tension via the catch-bond feedback mechanisms. We are unaware of techniques to estimate p_5, and set $p_5 = 1.25$. To test the sensitivity of our results with respect to p_5, we show that a 20% reduction of the sensitivity to actomyosin dissociation rate to tension, induces a higher unstable myosin equilibrium concentration $m_{eq.}$ (Figure S6). The overall dynamic evolution of the system, however, remains qualitatively unchanged as shown in Movie S16, to be compared with Figure 2 and Movie S2.
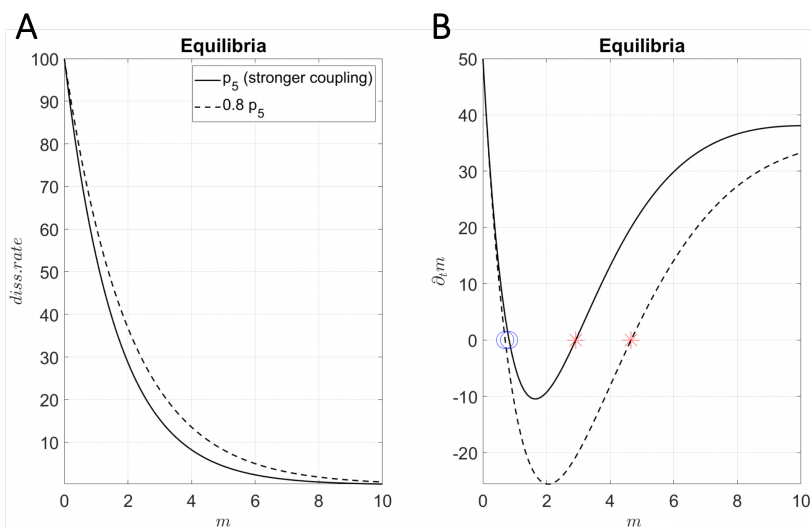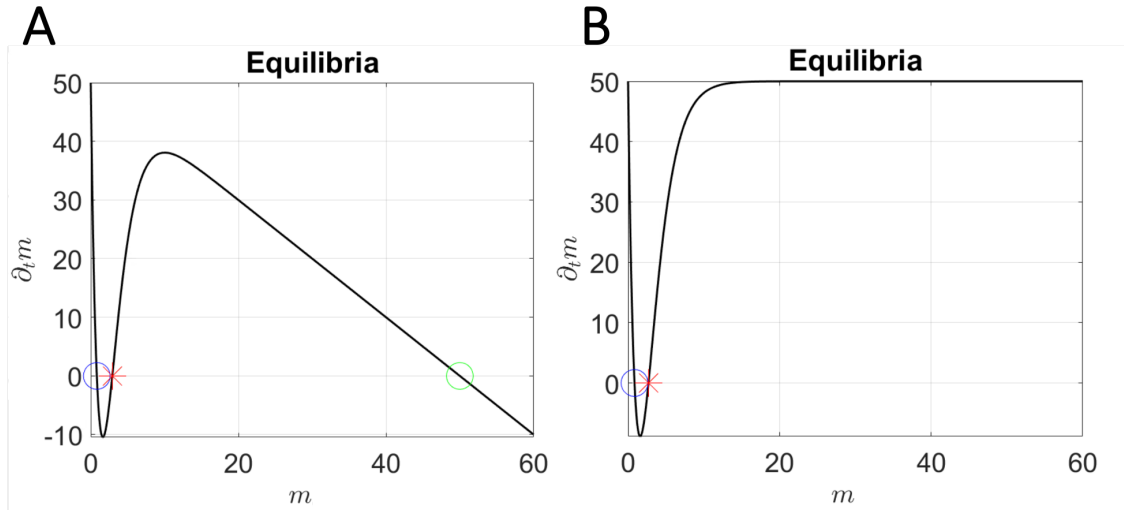

Supplementary Figure S6: **Sensitivity to p_5.** A) Exponential actomyosin dissociation rate $p_4 e^{-\frac{p_5}{2}m}$ for two values of p_5. B) Reducing p_5 by 20%, almost doubles the unstable m_{eq}.

By contrast, a 25% increase of p_5 causes a bifurcation of $m_{eq.}$, in which case model evolution differs considerably from experiments, as shown in Movie S17. Similar conclusions hold if changes in p_3 and p_4 induce a bifurcation of $m_{eq.}$. Our results, therefore, show that the active stress instability modulated by the catch-bond dynamics of actomyosin cables is essential for reproducing observed flow patterns.

4.3 p_6, p_7

While myosin activity cannot increase without bounds, the precise mechanisms by which and degree to which it saturates on junctions are beyond the scope of our model. This is because we are interested in a finite-time developmental interval characterized by instability rather than an asymptotic equilibrium state. To this end, we add a linear saturation

term $-p_6 m$ as the simplest functional form to dampen positive feedback and create a higher stable equilibrium value for m (Figure S3A and Figure S7A). For our model parameters, the three $m_{eq.}$ persist for $p_6 < 5.989$, preserving the instability needed for active stress intensity to grow. To show the robustness of our results with respect to changes in p_6, we show that even without ($p_6 = 0$) any saturation term (Figure S7B), the qualitative results of the 2D model do not change (Movie S18).

Supplementary Figure S7: **Sensitivity to p_6, controlling active stress intensity saturation.** Graphs of $p_3 - (p_4 e^{-\frac{p_5}{2} m} + p_6)m = 0$ for saturation parameter $p_6 = 1$ (A) and $p_6 = 0$ (B). Equilibria are marked with a blue circle (stable), red asterisk (unstable) and green circle (stable).

More generally, we find that slight variations in p_3, p_4, p_5, p_6 do not alter the overall system behavior as long as the graph (Figure S3A) determining m_{eq} does not change considerably (or undergoes a bifurcation).

Because the tissue is fluid-like and cells undergo embryo-scale motion, we argue that the advective transport of cells with active myosin dominates the induction of myosin via tension propagation on individual cables. Hence, we set $p_7 = 0.01$ throughout. Increasing the strength of active force propagation by 500% ($p_7 = 0.05$), the qualitative results of the 2D model (Movie S19) do not change, confirming the robustness of our results to parameters selection.

4.4 Boundary conditions

At the EP-EE boundary, the velocity is tangential to the boundary, ensuring that the EP area remains approximately constant over time, while in the EE region, the velocity is radial and roughly symmetric in α, explaining the expansion of the EE region over time (2). Because here we want to mechanistically predict what generates the observed flow patterns rather than enforcing it as an input, we do not select the boundary of our domain at the EP-EE interface, where the Dirichlet velocity boundary conditions would consist of a highly specific tangential flow profile. By contrast, we set our domain boundary $\partial \Omega$ (Figure 1A) slightly outside the EP-EE boundary, where, from the previous argument, the velocity is only radial and slightly higher than zero (we set $|\mathbf{v_b}| = 0.2$). Remarkably, our model recapitulates the correct vortical flows within the EP region and the associated tangential velocity behavior at the EP-EE interface. The most natural choice of boundary conditions for m, ϕ is no flux, as there is no experimental evidence of sources, sinks, or constant values of m, ϕ close to the EP-EE boundary. Mathematically, we set $\mathbf{v} = \mathbf{v_b}|_{\partial \Omega}, \nabla m \cdot \mathbf{n} = \mathbf{0}, \nabla \phi \cdot \mathbf{n} = \mathbf{0}$, where $\mathbf{n}$ is the outer normal to $\partial \Omega$.

To test the sensitivity of our results with respect to $|\mathbf{v_b}|$, we find that a 50% increase (decrease) of $|\mathbf{v_b}|$ does not affect the qualitative behavior of our results, as shown in Movie S20 (Movie S21) to be compared with Movie S2.

Overall, increasing (decreasing) $|\mathbf{v_b}|$ exerts a stronger (weaker) pulling of the PS towards the boundary.

4.5 Initial conditions

Consistent with experiments (Figure 1E at HH1), we set the initial orientation of actomyosin cables $\phi(\mathbf{x}, t_0)$ along the tangential direction, and $m(\mathbf{x}, t_0)$ as a Gaussian distribution (Figure 2C left) added to the unstable $m_{eq.}$ equilibrium (Figure S3A), modeling the onset of high active myosin in the mesendoderm sickle territory. The Gaussian

$$m(\mathbf{x}, t_0) = m_{eq.} + Ae^{-\frac{(r-r_c)^2}{2\sigma_r^2} - \frac{(\alpha-\alpha_c)^2}{2\sigma_\alpha^2}} \quad \text{(reduced mesendoderm)} \tag{S27}$$

is centered at $r_c = 0.6, \alpha_c = 250°$, has amplitude $A = 5$ and standard deviations $\sigma_r = 0.06, \sigma_\alpha = 3\sigma_r/r_c$. We select $\alpha_c = 250°$ to align the AP axis of the model (Figure 2C) with the AP axis from the experiment (Figure 2E). Changing α_c only changes the AP axis orientation. We set $\sigma_\alpha = 3\sigma_r/r_c$ so that the Gaussian width in the tangential direction is three times the width in the radial direction, reflecting the asymmetry of the mesendoderm sickle.

To test the sensitivity of our results to our Gaussian perturbation, we find that a 20% increase (decrease) in A Movie S22 (Movie S23) does not affect the qualitative behavior of our model. Similar conclusions hold for a 20% increase (decrease) in σ_r Movie S24 (Movie S25) and for 20% increase (decrease) in r_c Movie S26 (Movie S27). Increasing r_c causes a stronger pulling of the PS towards the boundary.

4.6 Summary

In all our simulations of (S26) (i.e. eq. 1 in the main text) producing different gastrulation modes (Figures 2-5), we use a single set of parameter values and boundary conditions, summarized in table 2, except for the initial myosin distribution $m(\mathbf{x}, t_0)$ and the scalar, constant parameter p_0, which controls the ratio of isotropic (ingression) to anisotropic (intercalation) active stresses, as described in detail in SI Sec. 1.4.2.

p_1	p_2	p_3	p_4	p_5	p_6	p_7	epiboly velocity $|\mathbf{v_b}|$
0.15	0.9	50	100	1.25	1	0.01	0.2

Table 2: Parameter values used in all two-dimensional simulations.

We change only p_0 and $m(\mathbf{x}, t_0)$. We set $p_0 = 2$ when there is active cell ingression and $p_0 = 0$ otherwise. Additionally, in the case of reduced mesendoderm precursors, we set $m(\mathbf{x}, t_0)$ as described in eq. (S27). By contrast, in the case of circular mesendoderm precursors (or ancestral condition), we use

$$m(\mathbf{x}, t_0) = m_{eq.} + Ae^{-\frac{(r-r_c)^2}{2\sigma_r^2}} \quad \text{(circular mesendoderm)} \tag{S28}$$

which models a Gaussian function of r, symmetric in α, added to the unstable $m_{eq.}$ and with the same parameters used in the wild type (Section 4.5). We summarize the combination of p_0 and $m(\mathbf{x}, t_0)$ to produce different gastrulation modes in Table 3.

gastrulation mode	p_0	$m(\mathbf{x}, t_0)$
Chick	2	reduced mesendoderm, eq.(S27)
Reptile	0	reduced mesendoderm, eq.(S27)
Teolost Fish	2	circular mesendoderm, eq.(S28)
Amphibian	0	circular mesendoderm, eq.(S28)

Table 3: Summary of p_0 and $m(\mathbf{x}, t_0)$ used to generate different gastrulation modes.

5 Comparison with other models

There is an increasing theoretical effort to couple mechanical and chemical signals in multicellular processes (*31, 32, 33, 34, 35, 36, 37, 3, 46, 38*). Our model has two main contributions. i) The tension-dependent dynamics of actomyosin cables (eqs. (S14),(S17)). ii) The coupling of tissue compressibility to tissue stress and active myosin (eq.(S6)). Regarding i), using a different argument in the context of active vertex models with no cell intercalations, (*37*) found for the first time that myosin recruitment along active edges must depend on the internal strain rate of the edge (or myosin cables) to guarantee the mechanical stability of the active tension network.

5.1 Differences with the tensile-ring model from (*3, 46*)

An alternative modeling approach for amniotic gastrulation is proposed in (*3, 46*) suggesting that a tensile ring at the EP-EE margin is sufficient to reproduce observation. We highlight below the main difference with our approach.

- Tensile ring model from (*3*) consists of a viscous flow

$$
\begin{cases}
\alpha \mathbf{\Delta v} = \nabla p + \mathbf{F_a}, \\
\nabla \cdot \mathbf{v} = \gamma, \quad \text{fitted from data in space and time,} \\
\mathbf{F_a} \text{ acts on a ring located at EP-EE margin, and is fitted from data in space and time.}
\end{cases} \tag{S29}
$$

Instead of fitting $\mathbf{F_a}$ over space and time, (*46*) propose a mechanistic model to evolve $\mathbf{F_a}$ at later times starting from an observed initial distribution.

By contrast, we model the fully coupled mechanochemical process and use information from experiments only at the initial time (eq. (S19)), hence providing a predictive mechanistic model. Specifically, we describe the process as a viscous flow

$$
\begin{cases}
\alpha \mathbf{\Delta v} = \nabla p + \mathbf{F_a}, \text{ first two eqs. in (S19),} \\
\nabla \cdot \mathbf{v} = \mathbf{g}(\mathbf{F_a}, \mathbf{v}, p), \text{ eq.(S6),} \\
\partial_t \mathbf{F_a} = \mathbf{f}(\mathbf{F_a}, \mathbf{v}), \text{ second two eqs. in (S19).}
\end{cases} \tag{S30}
$$

Using only experimental actomyosin cables distribution at the initial time (HH1) and predicting experimental observations over the following twelve hours (up to HH3) is an important difference compared to the procedure proposed in (*3*) that requires data fitting over space and time.

- The active force $\mathbf{F_a}$ in (*3*) acts only on a ring centered at the EP-EE margin. By contrast, we model $\mathbf{F_a}$ in the whole embryo because actomyosin cables generating $\mathbf{F_a}$ are abundantly distributed and evolve dynamically within the embryo consistent with experimental observations (Figure 1). At stages after HH1, experiments show that active myosin is dominant along the PS rather than on the EP-EE boundary (Figures 1D-E), consistent with our model prediction (Figure 2C). To support further this finding, in Figure 3 we show $\mathbf{F_a}$ inferred from PIV velocity and eq. (S19) at HH3. The active forces are mainly perpendicular to the PS (Figures 3) rather than being organized on a ring-shaped structure.

- (*3, 46*) do not address the forces that drive γ (eq. (S29)), which is fitted from data. By contrast, our model (eq. (S30)) explains and predicts them in time as a response to mechanical stress, recapitulating the flow divergence and areal changes that we see in experiments (Figures 2F-H), as well as the overall Dynamic Morpphoskeletons and other Lagrangian metrics (Figure 2 and Movies 2-3).

Our ability to predict four different perturbations in addition to the wild-type development (Figs. 2,4 and Movies 2-12) supports the validity of our model and hence the underlying biological hypothesis.

6 The Dynamic Morphoskeletons quantify morphogenetic flows

To quantify spatio-temporal flows, we use the notion of Lagrangian coherent structures (*59*) adapted to morphogenesis, i.e. the the embryo's dynamic morphoskeletons (DM) (*44*). The DM is based on a Lagrangian description (Figure S8A) of tissue deformation captured by Finite Time Lyapunov Exponents (FTLE), which naturally combine local and global mechanisms along cell trajectories. The DM consists of attractors and repellers toward which cells converge or diverge over a specific time interval $T = t_f - t_0$. Repellers are marked by high values of the forward FTLE $\Lambda_{t_0}^{t_f}(\mathbf{x}_0)$; attractors are marked by high values of backward FTLE $\Lambda_{t_f}^{t_0}(\mathbf{x}_f)$ and their domain of attraction (DOA) by high values of the backward FTLE displayed on the initial cell positions $\Lambda_{t_f}^{t_0}(\mathbf{x}_0)$ (see Figure S8B for an illustration). The DM is objective, reveals the intrinsic geometric feature of spatio-temporal trajectories and is robust to noise (*44*), hence it is ideal for quantifying morphogenesis and comparing models with experiments.
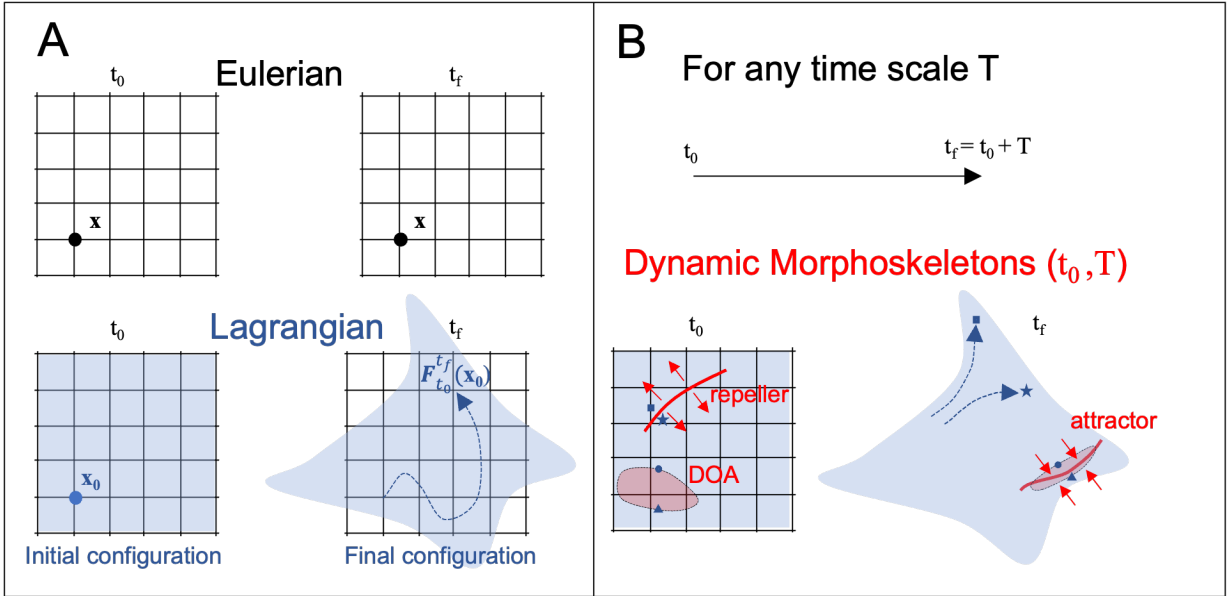
Supplementary Figure S8: **The Dynamic Morphoskeletons (*44*) quantify morphogenetic flows.** A) Eulerian coordinates $\mathbf{x}$ describe fixed spatial locations, while Lagrangian coordinates $\mathbf{x}_0$ label the identity of cells or tissue regions at their initial position and follow their trajectories $\mathbf{F}_{t_0}^{t_f}(x_0)$ over time. B) Fix the initial time t_0 of the Lagrangian analysis, which we consider to be the beginning of our experiments (developmental stage HH1). For any Lagrangian time scale T, the Dynamic Morphoskeletons consist of repellers, attractors and Domain of Attractions (DOA). Repellers mark regions at the initial cell configuration $\mathbf{x}_0$ such that nearby cells (star and square markers) at opposite sides of the repeller will separate by the final time t_f. Attractors mark regions at the final cell configuration $\mathbf{x}_f$ such that initially far cells (triangle and circle markers) will converge to the attractor by the final time t_f. The DOA (red area) marks the initial position of all the cells that will converge to the attractor by t_f.

Given a modelled or experimental planar velocity field $\mathbf{v}(\mathbf{x}, t)$, we compute the Dynamic Morphoskeleton (DM) (*44*) from the backward and forward Finite Time Lyapunov Exponents (FTLE). We compute the FTLE as

$$\Lambda_{t_0}^{t_f}(\mathbf{x}_0) = \frac{\ln\left(\lambda_2(\mathbf{x}_0)\right)}{|t_f - t_0|}, \quad \mathbf{x}_f := \mathbf{F}_{t_0}^{t_f}(\mathbf{x}_0) = \mathbf{x}_0 + \int_{t_0}^{t_f} \mathbf{v}(\mathbf{F}_{t_0}^{\tau}(\mathbf{x}_0), \tau)\, d\tau, \tag{S31}$$

where $\lambda_2(\mathbf{x}_0)$ denotes the highest singular value of the Jacobian of the flow map $\nabla \mathbf{F}_{t_0}^{t_f}(\mathbf{x}_0)$ and $\mathbf{F}_{t_0}^{t_f}(\mathbf{x}_0)$ the flow map describing the trajectories from their initial $\mathbf{x}_0$ to final $\mathbf{x}_f$ positions. To compute the FTLE, we first calculate $\mathbf{F}_{t_0}^{t}(\mathbf{x}_0)$ by integrating the cell velocity field $\mathbf{v}(\mathbf{x}, t)$ using the MATLAB built-in Runge-Kutta solver ODE45 with absolute and relative tolerance of 10^{-6}, linear interpolation in space and time, and a uniform dense grid of initial conditions. Then,

denoting the $i-th$ component of the flow map $\mathbf{F}_{t_0}^t(\mathbf{x}_0)$ by $x^i(x_0^1, x_0^2, t_0, t)$, we compute the deformation gradient $\nabla \mathbf{F}_{t_0}^t(\mathbf{x}_0)$ using the finite-difference approximation

$$\nabla \mathbf{F}_{t_0}^t(\mathbf{x}_0) \approx \left[\begin{array}{cc} \frac{x^1(x_0^1+\delta, x_0^2, t_0, t) - x^1(x_0^1-\delta, x_0^2, t_0, t)}{2\delta} & \frac{x^1(x_0^1, x_0^2+\delta, t_0, t) - x^1(x_0^1, x_0^2-\delta, t_0, t)}{2\delta} \\ \frac{x^2(x_0^1+\delta, x_0^2, t_0, t) - x^2(x_0^1-\delta, x_0^2, t_0, t)}{2\delta} & \frac{x^2(x_0^1, x_0^2+\delta, t_0, t) - x^2(x_0^1, x_0^2-\delta, t_0, t)}{2\delta} \end{array} \right], \tag{S32}$$

where δ is the initial conditions' grid spacing. After computing $\nabla \mathbf{F}_{t_0}^t(\mathbf{x}_0)$, we use eq. (S31) for computing the FTLE field.
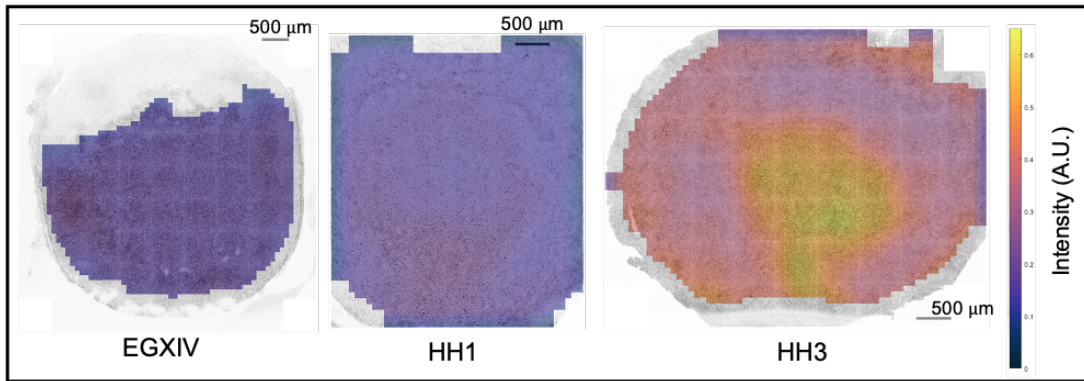
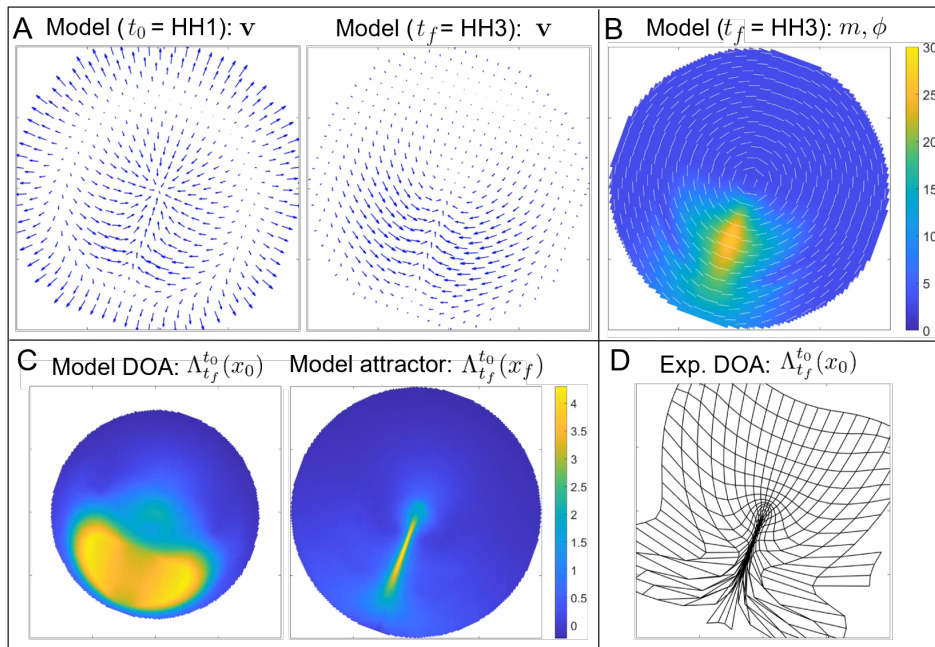# 7   Additional supplementary figures
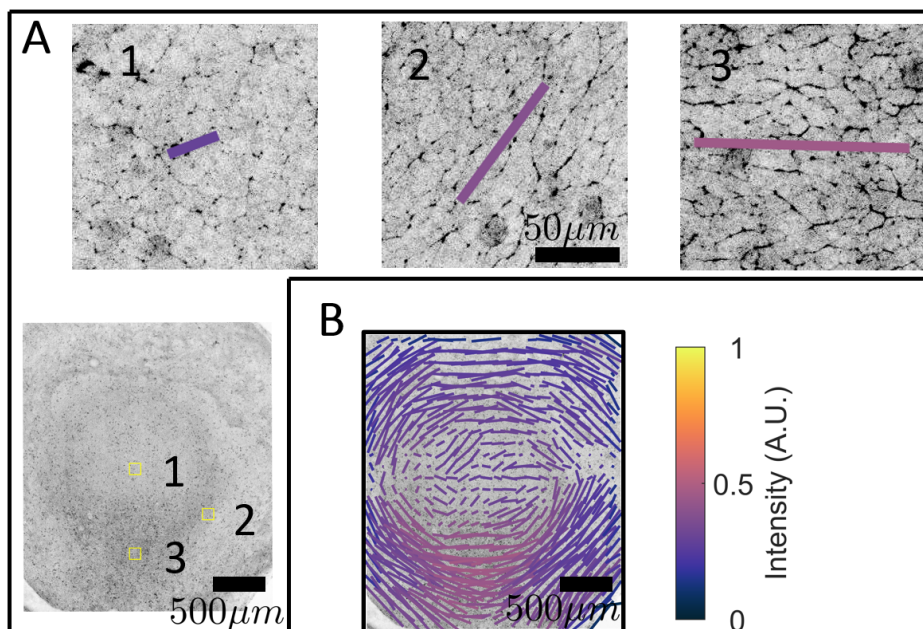
Supplementary Figure S9: **Actomyosin cables quantification.** A) Phospho-myosin light chain (pMLC) expression in the chick gastrula (HH1). Panels 1-3, taken at the positions of the yellow squares in the overview image, show the formation of pMLC cables spanning several cells. The length and orientation of the bars in panels 1-3 quantify the anisotropy and orientation of the pMLC cables, and the color of the bars indicates the pMLC concentration. B) The pattern of pMLC cables of the HH1 stage embryo shown in A. The alignment and the orientation of the active myosin cables are quantified from the asymmetry of the Fourier power spectrum (*11*), calculated in a tiling pattern over the embryo, while myosin intensity is calculated as average intensity in the same tiles. For experimental details, see the accompanying paper (*4*).

8   Additional model perturbations

In this section, we show the effects of additional model perturbations that provide insight into the role of p_1 and $\mathbf{m}(\mathbf{x}, t_0)$. All other parameters and initial and boundary conditions are the same as WT. First, by increasing the ratio of shear to bulk viscosity (p_1), the polonaise movements are lost (Figure S11A), resembling instead the impaired gastrulation movements experimentally observed in the absence of cell division (*60, 61*). We reason that, at leading order, impairing cell divisions reduces fluidity, which is captured by the increase of tissue-scale shear viscosity μ, and hence p_1 (*62*).

Supplementary Figure S10: **Quantification of active myosin via pMLC intensity.** The pattern of pMLC intensity evolves in time, as in Figure 1E. Color represents absolute measured signal intensity (arbitrary units). Changes in absolute pMLC intensity show a global increase in active myosin as gastrulation progresses, particularly from HH1 to HH3. This increase is consistent with the active stress instability predicted by our model (Figure 2). For experimental details, see the accompanying paper (*4*).

Supplementary Figure S11: **A higher ratio p_1 of shear and bulk viscosity destroys polonaise movements.** Model output with a higher $p_1 = 0.5$. A) Initial (t_0) and final (t_f) velocity field. B) Final (t_f) distribution of m, ϕ. C) Model-based DOA at t_0 (HH1) and the attractor at t_f (HH3). D) Deformed Lagrangian grid from the predicted model velocity. Units are non-dimensional.

Next, we vary the angular extent (σ_α) of the initial mesendoderm, encoded in $\mathbf{m}(\mathbf{x}, t_0)$. When σ_α is much smaller, a streak forms, but the attractor is shorter and its DOA is far smaller than WT (Figure S12A-D). By instead increasing σ_α, the reduced mesendoderm initial condition (eq. (S27)) can be gradually transformed into the circular mesendoderm initial condition (eq. (S28)). Figure S12E-H showcases the model predictions for an intermediate initial condition ($\sigma_\alpha = 0.8$). Here, active stress intensity is initialized in a ring with much greater stress in the posterior. While polonaise movements are generated and maintained, the DM (S12G) lacks a sharp attractor while having a large DOA caused by excessive contractile activity in the embryo, differing substantially from WT. These results suggest that the finite width of the mesendoderm precursor cells at HH1 (see experiments in Fig. 1E) is important

for generating the correct gastrulation flows. The finite extent of the mesendoderm precursor cells is generated by a molecular patterning of the embryo before HH1 (*5*).
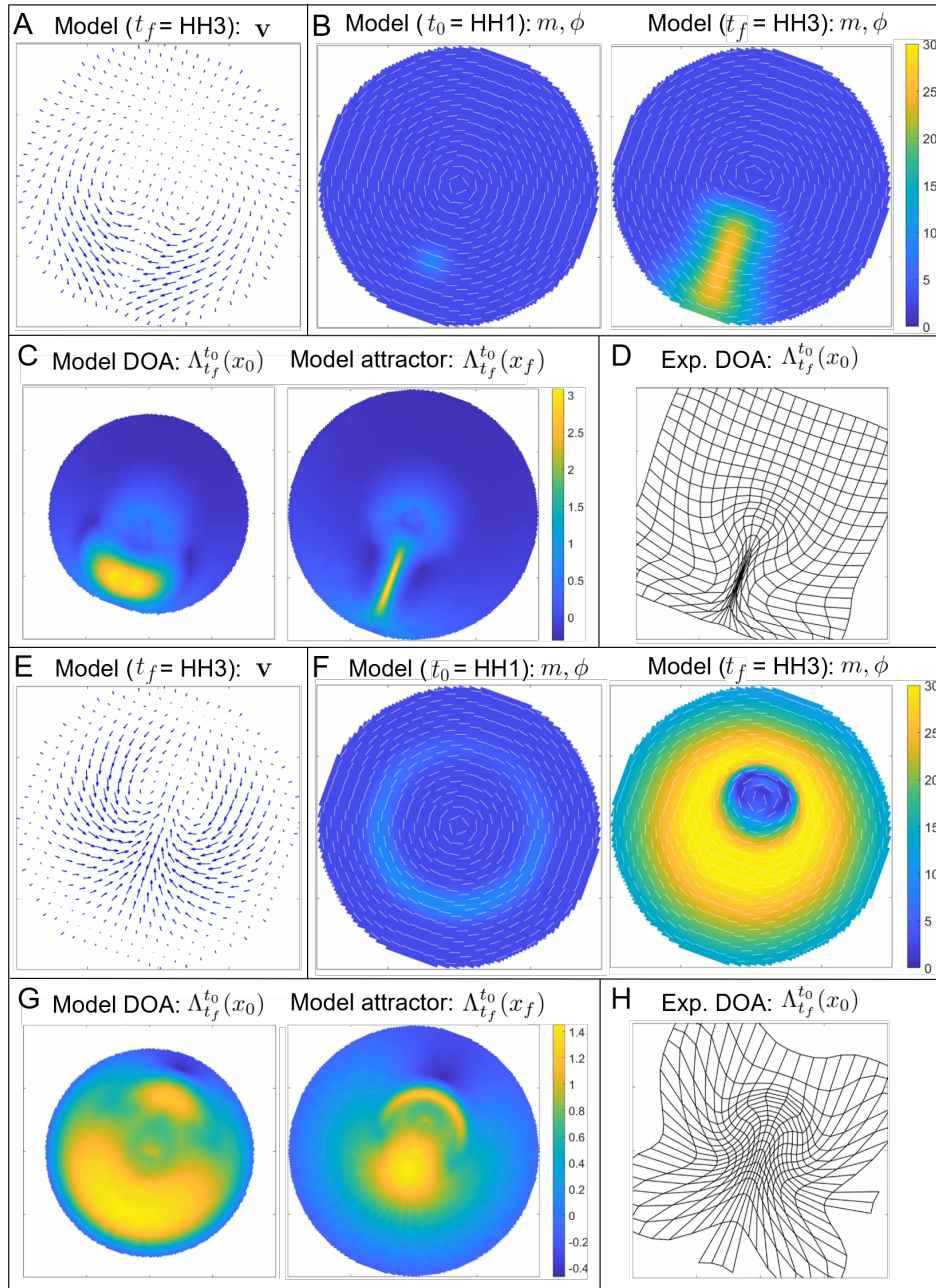
Supplementary Figure S12: **Effect of extent of initial mesendoderm.** Model output from initial conditions with a smaller mesendoderm $\sigma_\alpha = \sigma_r = 0.06$ (A-D) and an intermediate mesendoderm $\sigma_\alpha = 0.8$ (E-H) between the reduced mesendoderm and circular mesendoderm initial conditions. A,E) Final (t_f) velocity fields. B,F) Initial (t_0) and final (t_f) distributions of m, ϕ. C,G) Model-based DOA at t_0 (HH1) and the attractor at t_f (HH3). D,H) Deformed Lagrangian grids from the predicted model velocity. Units are non-dimensional.

Finally, we show instances in which two streaks form, either spontaneously or induced by implantation of Vg1 (GDF3) secreting cells (*63*). In this case, distinct streaks either maintain their separation or fuse. In the first case,

we initialize two reduced mesendoderms $180°$ apart. Unlike the ordinary twin perturbation, the model predicts that these two streaks will not fuse but will instead halt each other's extension from posterior to anterior and vice-versa S13A-D). In the second case, we nitialize two reduced mesendoderms $90°$ apart and reduce the amplitude to $A = 0.1$ for one of them. Despite the smaller reduced mesendoderm's weaker convergent extension, which is apparent in lower scalar values of its corresponding attractor (S13G), it causes the stronger streak to bend away from it, as in the ordinary twin perturbation.
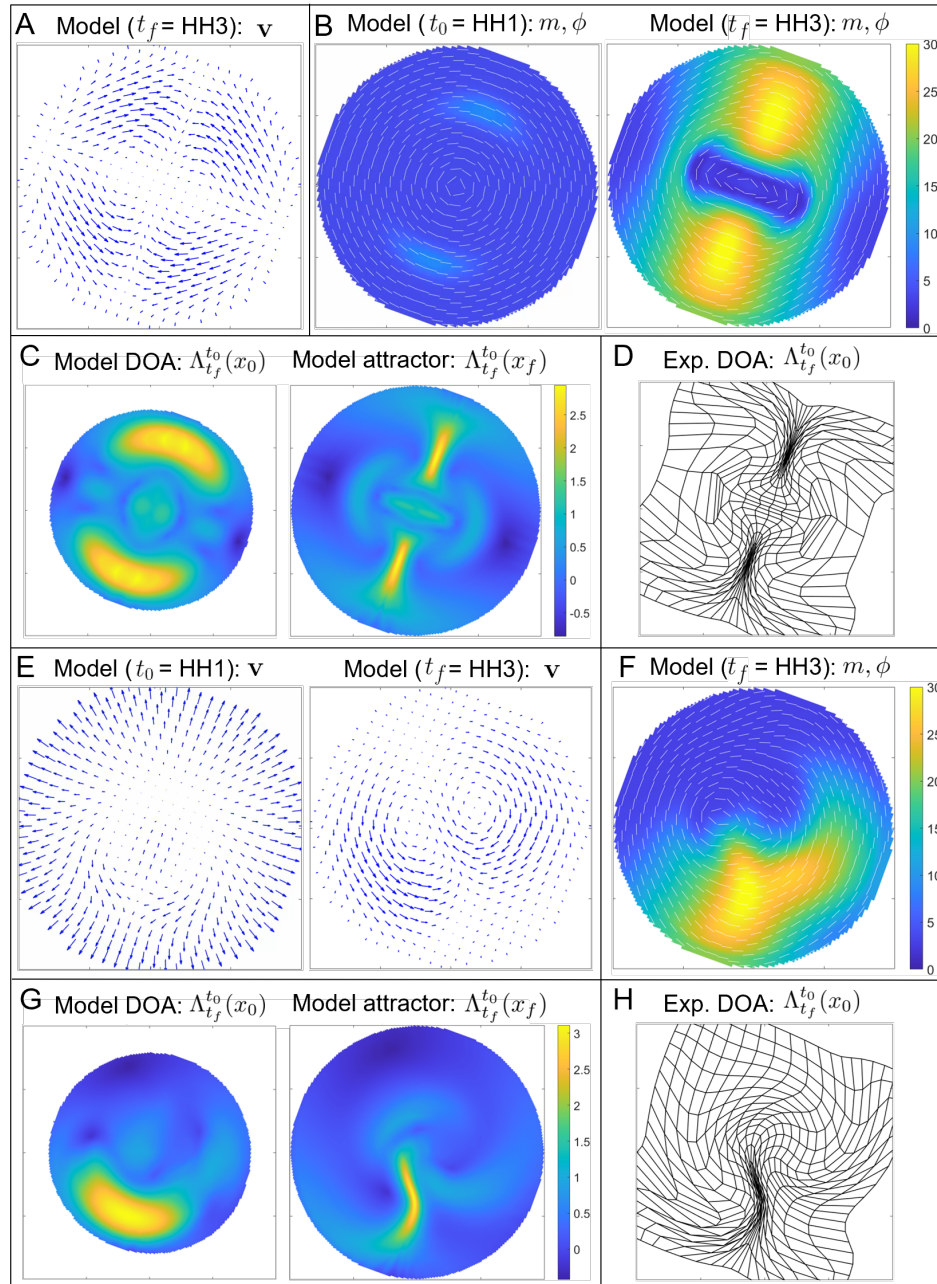
Supplementary Figure S13: **Multiple streaks.** Model output from initial conditions with two reduced mesendoderms oriented $180°$ apart (A-D) and $90°$ apart (E-H). A) Final (t_f) velocity field. B) Initial (t_0) and final (t_f) distributions of m, ϕ. C,G) Model-based DOA at t_0 (HH1) and the attractor at t_f (HH3). D,H) Deformed Lagrangian grids from the predicted model velocity. E) Initial (t_0) and final (t_f) velocity field. F) Final (t_f) distribution of m, ϕ. Units are non-dimensional.

Supplementary movies

Movie S1: Time evolution movie associated with Fig. 2B.
Movie S2: Time evolution movie associated with Figs. 2C-D.
Movie S3: Time evolution movie associated with Fig. 2E.
Movie S4: Time evolution movie associated with Fig. 4A.
Movie S5: Time evolution movie associated with Fig. 4B.
Movie S6: Time evolution movie associated with Fig. 4C.
Movie S7: Time evolution movie associated with Fig. 4D.
Movie S8: Time evolution movie associated with Fig. 4E.
Movie S9: Time evolution movie associated with Fig. 4F.
Movie S10: Deforming Lagrangian grid overlaid on the light-sheet microscope images corresponding to the experimental data used in Movie S9.
Movie S11: Time evolution movie associated with Fig. 4G.
Movie S12: Time evolution movie associated with Fig. 4H.
Movie S13: Time evolution movie associated with Fig. S1C.
Movie S14: Sensitivity to p_2. Same as Movie S2, but using a lower value of the parameter p_2.
Movie 15: Sensitivity to p_2. Same as Movie S2, but using a higher value of the parameter p_2.
Movie S16: Sensitivity to p_5. Same as Movie S2, but using a lower value of the parameter p_5.
Movie S17: Sensitivity to p_5. Same as Movie S2, but using a higher value of the parameter p_5.
Movie S18: Sensitivity to p_6. Same as Movie S2, but setting $p_6 = 0$.
Movie S19: Sensitivity to p_7. Same as Movie S2, but using a higher value of the parameter p_7.
Movie S20: Sensitivity to the epiboly velocity $|\mathbf{v_b}|$. Same as Movie S2, but using a higher value of $|\mathbf{v_b}|$.
Movie S21: Sensitivity to the epiboly velocity $|\mathbf{v_b}|$. Same as Movie S2, but using a lower value of $|\mathbf{v_b}|$.
Movie S22: Sensitivity to the amplitude A of the Gaussian perturbation added to the unstable m equilibrium. Same as Movie S2, but using a higher A.
Movie S23: Sensitivity to the amplitude A of the Gaussian perturbation added to the unstable m equilibrium. Same as Movie S2, but using a lower A.
Movie S24: Sensitivity to the radial standard deviation σ_r of the Gaussian perturbation added to the unstable m equilibrium. Same as Movie S2, but using a higher σ_r.
Movie S25: Sensitivity to the radial standard deviation σ_r of the Gaussian perturbation added to the unstable m equilibrium. Same as Movie S2, but using a lower σ_r.
Movie S26: Sensitivity to the radial mean r_c of the Gaussian perturbation added to the unstable m equilibrium. Same as Movie S2, but using a higher r_c.
Movie S27: Sensitivity to the radial mean r_c of the Gaussian perturbation added to the unstable m equilibrium. Same as Movie S2, but using a lower r_c.

REFERENCES AND NOTES

1. C. D. Stern, *Gastrulation: From Cells to Embryo* (CSHL Press, 2004).

2. E. Rozbicki, M. Chuai, A. I. Karjalainen, F. Song, H. M. Sang, R. Martin, H. J. Knölker, M. P. MacDonald, C. J. Weijer, Myosin-II-mediated cell shape changes and cell intercalation contribute to primitive streak formation. *Nat. Cell Biol.* **17**, 397–408 (2015).

3. M. Saadaoui, D. Rocancourt, J. Roussel, F. Corson, J. Gros, A tensile ring drives tissue flows to shape the gastrulating amniote embryo. *Science* **367**, 453–458 (2020).

4. M. Chuai, G. Serrano Nájera, M. Serra, L. Mahadevan, C. J. Weijer, Reconstruction of distinct vertebrate gastrulation modes via modulation of key cell behaviors in the chick embryo. *Sci. Adv.* **9**, eabn5429 (2023).

5. G. Serrano Nájera, C. J. Weijer, Cellular processes driving gastrulation in the avian embryo. *Mech. Dev.* **163**, 103624 (2020).

6. O. Voiculescu, F. Bertocchini, L. Wolpert, R. E. Keller, C. D. Stern, The amniote primitive streak is defined by epithelial cell intercalation before gastrulation. *Nature* **449**, 1049–1052 (2007).

7. Y. Nakaya, E. W. Sukowati, Y. Wu, G. Sheng, RhoA and microtubule dynamics control cell–basement membrane interaction in EMT during gastrulation. *Nat. Cell Biol.* **10**, 765–775 (2008).

8. O. Voiculescu, L. Bodenstein, I.-J. Lau, C. D. Stern, Local cell interactions and self-amplifying individual cell ingression drive amniote gastrulation. *eLife* **3**, e01817 (2014).

9. L. Gräper, Die Primitiventwicklung des Hühnchens nach stereokinematographischen Untersuchungen, kontrolliert durch vitale Farbmarkierung und verglichen mit der Entwicklung anderer Wirbeltiere. *Wilhelm Roux Arch. Entwickl. Mech. Org.* **116**, 382–429 (1929).

10. M. Chuai, W. Zeng, X. Yang, V. Boychenko, J. A. Glazier, C. J. Weijer, Cell movement during chick primitive streak formation. *Dev. Biol.* **296**, 137–149 (2006).

11. M. Durande, S. Tlili, T. Homan, B. Guirao, F. Graner, H. Delanoë-Ayari, Fast determination of coarse-grained cell anisotropy and size in epithelial tissue images using Fourier transform. *Phys. Rev. E* **99**, 062401 (2019).

12. C. Bertet, L. Sulak, T. Lecuit, Myosin-dependent junction remodelling controls planar cell intercalation and axis elongation. *Nature* **429**, 667–671 (2004).

13. J. T. Blankenship, S. T. Backovic, J. S. Sanny, O. Weitz, J. A. Zallen, Multicellular rosette formation links planar cell polarity to tissue morphogenesis. *Dev. Cell* **11**, 459–470 (2006).

14. J. A. Zallen, E. Wieschaus, Patterned gene expression directs bipolar planar polarity in drosophila. *Dev. Cell* **6**, 343–355 (2004).

15. J. Lavalou, Q. Mao, S. Harmansa, S. Kerridge, A. C. Lellouch, J.-M. Philippe, S. Audebert, L. Camoin, T. Lecuit, Formation of polarized contractile interfaces by self-organized Toll-8/Cirl GPCR asymmetry. *Dev. Cell* **56**, 1574–1588 (2021).

16. A. Munjal, J.-M. Philippe, E. Munro, T. Lecuit, A self-organized biomechanical network drives shape changes during tissue morphogenesis. *Nature* **524**, 351–355 (2015).

17. M. Rauzi, U. Krzic, T. E. Saunders, M. Krajnc, P. Ziherl, L. Hufnagel, M. Leptin, Embryo-scale tissue mechanics during Drosophila gastrulation movements. *Nat. Commun.* **6**, 8677 (2015).

18. S. J. Streichan, M. F. Lefebvre, N. Noll, E. F. Wieschaus, B. I. Shraiman, Global morphogenetic flow is accurately predicted by the spatial distribution of myosin motors. *eLife* **7**, e27454 (2018).

19. A. Bailles, C. Collinet, J. M. Philippe, P. F. Lenne, E. Munro, T. Lecuit, Genetic induction and mechanochemical propagation of a morphogenetic wave. *Nature* **572**, 467–473 (2019).

20. F. J. Vernerey, U. Akalp, Role of catch bonds in actomyosin mechanics and cell mechanosensitivity. *Phys. Rev. E* **94**, 012403 (2016).

21. R. Fernandez-Gonzalez, S. de Matos Simoes, J.-C. Röper, S. Eaton, J. A. Zallen, Myosin II dynamics are regulated by tension in intercalating cells. *Dev. Cell* **17**, 736–743 (2009).

22. J. M. Laakso, J. H. Lewis, H. Shuman, E. M. Ostap, Myosin I can act as a molecular force sensor. *Science* **321**, 133–136 (2008).

23. C. Veigel, J. E. Molloy, S. Schmitz, J. Kendrick-Jones, Load-dependent kinetics of force production by smooth muscle myosin measured with optical tweezers. *Nat. Cell Biol.* **5**, 980–986 (2003).

24. W. E. Thomas, V. Vogel, E. Sokurenko, Biophysics of catch bonds. *Annu. Rev. Biophys.* **37**, 399–416 (2008).

25. M. C. Marchetti, J. F. Joanny, S. Ramaswamy, T. B. Liverpool, J. Prost, M. Rao, R. A. Simha, Hydrodynamics of soft active matter. *Rev. Mod. Phys.* **85**, 1143–1189 (2013).

26. F. Graner, J. A. Glazier, Simulation of biological cell sorting using a two-dimensional extended Potts model. *Phys. Rev. Lett.* **69**, 2013–2016 (1992).

27. A. G. Fletcher, M. Osterfield, R. E. Baker, S. Y. Shvartsman, Vertex models of epithelial morphogenesis. *Biophys. J.* **106**, 2291–2304 (2014).

28. S. Alt, P. Ganguly, G. Salbreux, Vertex models: From cell mechanics to tissue morphogenesis. *Philos. Trans. R. Soc. Lond. B Biol. Sci.* **372**, 20150520 (2017).

29. A. Bonfanti, J. L. Kaplan, G. Charras, A. Kabla, Fractional viscoelastic models for power-law materials. *Soft Matter* **16**, 6002–6020 (2020).

30. R. Alert, X. Trepat, Physical models of collective cell migration. *Annu. Rev. Condens. Matter Phys.* **11**, 77–101 (2020).

31. C. Collinet, T. Lecuit, Programmed and self-organized flow of information during morphogenesis. *Nat. Rev. Mol. Cell Biol.* **22**, 245–265 (2021).

32. Y. Maroudas-Sacks, K. Keren, Mechanical patterning in animal morphogenesis. *Annu. Rev. Cell Dev. Biol.* **37**, 469–493 (2021).

33. B. Ladoux, R.-M. Mège, Mechanobiology of collective cell behaviours. *Nat. Rev. Mol. Cell Biol.* **18**, 743–757 (2017).

34. R. Etournay, M. Popović, M. Merkel, A. Nandi, C. Blasse, B. Aigouy, H. Brandl, G. Myers, G. Salbreux, F. Jülicher, S. Eaton, Interplay of cell dynamics and epithelial tension during morphogenesis of the Drosophila pupal wing. *eLife* **4**, e07090 (2015).

35. H. J. Gustafson, N. Claussen, S. De Renzis, S. J. Streichan, Patterned mechanical feedback establishes a global myosin gradient. *Nat. Commun.* **13**, 7050 (2022).

36. N. A. Dye, M. Popović, K. V. Iyer, J. F. Fuhrmann, R. Piscitello-Gómez, S. Eaton, F. Jülicher, Self-organized patterning of cell morphology via mechanosensitive feedback. *eLife* **10**, e57964 (2021).

37. N. Noll, M. Mani, I. Heemskerk, S. J. Streichan, B. I. Shraiman, Active tension network model suggests an exotic mechanical state realized in epithelial tissues. *Nat. Phys.* **13**, 1221–1226 (2017).

38. A.-C. Reymann, F. Staniscia, A. Erzberger, G. Salbreux, S. W. Grill, Cortical flow aligns actin filaments to form a furrow. *eLife* **5**, e17807 (2016).

39. E. W. Gehrels, B. Chakrabortty, M.-E. Perrin, M. Merkel, T. Lecuit, Curvature gradient drives polarized tissue flow in the *Drosophila embryo*. *Proc. Natl. Acad. Sci. U.S.A.* **120**, e2214205120 (2023).

40. A. Ioratim-Uba, T. B. Liverpool, S. Henkes, Mechano-chemical active feedback generates convergence extension in epithelial tissue. arXiv:2303.02109 (2023). https://doi.org/10.48550/arXiv.2303.02109.

41. M. Valet, E. D. Siggia, A. H. Brivanlou, Mechanical regulation of early vertebrate embryogenesis. *Nat. Rev. Mol. Cell Biol.* **23**, 169–184 (2021).

42. G. Jeffery, The motion of ellipsoidal particles immersed in a viscous fluid. *Proc. R. Soc. Lond.* **102**, 161–179 (1922).

43. C. Truesdell, W. Noll, *The Non-Linear Field Theories of Mechanics* (Springer, 2004).

44. M. Serra, S. Streichan, M. Chuai, C. J. Weijer, L. Mahadevan, Dynamic morphoskeletons in development. *Proc. Natl. Acad. Sci. U. S. A.* **117**, 11444–11449 (2020).

45. G. Serrano Nájera, C. J. Weijer, The evolution of gastrulation morphologies. *Development* **150**, dev200885 (2023).

46. P. Caldarelli, A. Chamolly, O. Alegria-Prévot, J. Gros, F. Corson, Self-organized tissue mechanics underlie embryonic regulation. bioRxiv 2021.10.08.463661 (2021). https://doi.org/10.1101/2021.10.08.463661.

47. R. Feroze, J. H. Shawky, M. von Dassow, L. A. Davidson, Mechanics of blastopore closure during amphibian gastrulation. *Dev. Biol.* **398**, 57–67 (2015).

48. D. R. Shook, E. M. Kasprowicz, L. A. Davidson, R. Keller, Large, long range tensile forces drive convergence during Xenopus blastopore closure and body axis elongation. *eLife* **7**, e26944 (2018).

49. M. Valet, E. D. Siggia, A. H. Brivanlou, Mechanical regulation of early vertebrate embryogenesis. *Nat. Rev. Mol. Cell Biol.* **23**, 169–184 (2022).

50. A. Carmany-Rampey, A. F. Schier, Single-cell internalization during zebrafish gastrulation. *Curr. Biol.* **11**, 1261–1265 (2001).

51. S. F. Gabriel Krens, J. H. Veldhuis, V. Barone, D. Čapek, J.-L. Maître, G. W. Brodland, C.-P. Heisenberg, Interstitial fluid osmolarity modulates the action of differential tissue surface tension in progenitor cell segregation during gastrulation. *Development* **144**, 1798–1806 (2017).

52. R. Fernandez-Gonzalez, S. de Matos Simoes, J.-C. Röper, S. Eaton, J. A. Zallen, Myosin II dynamics are regulated by tension in intercalating cells. *Dev. Cell* **17**, 736–743 (2009).

53. R. Clément, B. Dehapiot, C. Collinet, T. Lecuit, P.-F. Lenne, Viscoelastic dissipation stabilizes cell shape changes during tissue morphogenesis. *Curr. Biol.* **27**, 3132–3142.e4 (2017).

54. V. Ferro, M. Chuai, D. McGloin, C. J. Weijer, Measurement of junctional tension in epithelial cells at the onset of primitive streak formation in the chick embryo via non-destructive optical manipulation. *Development* **147**, dev175109 (2020).

55. M. F. Staddon, K. E. Cavanaugh, E. M. Munro, M. L. Gardel, S. Banerjee, Mechanosensitive junction remodeling promotes robust epithelial morphogenesis. *Biophys. J.* **117**, 1739–1750 (2019).

56. T. Chung, *Computational Fluid Dynamics* (Cambridge Univ. Press, 2012).

57. J. S. Bois, F. Jülicher, S. W. Grill, Pattern formation in active fluids. *Phys. Rev. Lett.* **106**, 028103 (2011).

58. R. Sknepnek, I. Djafer-Cherif, M. Chuai, C. Weijer, S. Henkes, Generating active T1 transitions through mechanochemical feedback. *eLife* **12**, e79862 (2023).

59. G. Haller, Lagrangian coherent structures. *Annu. Rev. Fluid. Mech.* **47**, 137–162 (2015).

60. C. Cui, X. Yang, M. Chuai, J. A. Glazier, C. J. Weijer, Analysis of tissue flow patterns during primitive streak formation in the chick embryo. *Dev. Biol.* **284**, 37–47 (2005).

61. J. Firmino, D. Rocancourt, M. Saadaoui, C. Moreau, J. Gros, Cell division drives epithelial cell rearrangements during gastrulation in chick. *Dev. Cell* **36**, 249–261 (2016).

62. J. Ranft, M. Basan, J. Elgeti, J. F. Joanny, J. Prost, F. Jülicher, Fluidization of tissues by cell division and apoptosis. *Proc. Natl. Acad. Sci. U. S. A.* **107**, 20863–20868 (2010).

63. S. B. Shah, I. Skromne, C. R. Hume, D. S. Kessler, K. J. Lee, C. D. Stern, J. Dodd, Misexpression of chick Vg1 in the marginal zone induces primitive streak formation. *Development* **124**, 5127–5138 (1997).